Role of inter-chain tunneling in an extended Bose-Hubbard ladder

A Thesis

submitted to
Indian Institute of Science Education and Research Pune
in partial fulfillment of the requirements for the
BS-MS Dual Degree Programme

by

Gopal Chandra Santra

Indian Institute of Science Education and Research Pune
Dr. Homi Bhabha Road,
Pashan, Pune 411008, INDIA.

July, 2021

Supervisor: Dr. Rejish Nath

© Gopal Chandra Santra 2021
All rights reserved

Certificate

This is to certify that this dissertation entitled “Role of inter-chain tunneling in an extended Bose-Hubbard ladder ” towards the partial fulfilment of the BS-MS dual degree programme at the Indian Institute of Science Education and Research, Pune represents study/work carried out by Gopal Chandra Santra at Indian Institute of Science Education and Research under the supervision of Dr. Rejish Nath, Associate Professor, Department of Physics , during the academic year 2016-2021.

Dr. Rejish Nath

Committee:
Dr. Rejish Nath
Dr. Sreejith GJ

This thesis is dedicated to all my well-wishers and Him,

Declaration

I hereby declare that the matter embodied in the report entitled “Role of inter-chain tunneling in an extended Bose-Hubbard ladder ”, are the results of the work carried out by me at the Department of Physics, Indian Institute of Science Education and Research, Pune, under the supervision of Dr. Rejish Nath and the same has not been submitted elsewhere for any other degree.

Gopal Chandra Santra

Gopal Chandra Santra

Acknowledgments

At the end of 2018, when I was confused about what part of physics I like and should pursue in the future, Ratheejit-da suggested I join Dr. Rejish Nath's group. Although I started with quantum optics, I could not but shifted to many-body physics after the exciting stat-mech course by Dr. Sreejith GJ. And in no way do I want to turn back.

Interesting group meetings, enthusiastic peers like Ratheejit, Sandra, Yashwant, Ankita, and long zoom calls with Dr. Nath kept the research life at pandemic untouched. His excitement with the new results and support for my crazy ideas made me more dedicated than ever. He is the kind of person who will always motivate you to get more skills than knowledge. And, if I have learned something about research strategies, he is primarily liable for it. I acknowledge the IISER Pune supercomputing facility as all the computations are conducted using it.

Since I joined IISER, the last five years have been the most beautiful time of my life - amazing friends, professors, and culture on the campus. Informal and interdisciplinary learning, random discussions at the dinner table, incredible seniors, and group study before the exam night are indelible. I should never acknowledge my small gangs- Arijit, Writam, Wridhdhi, and Sounak, for their terrible food choices, gaming night, and to make us rarely pass in HSS. Who wants to be luckier than to have Viraj, Aagam, Shriya, Sagnik, Sounak, Onkar, Vighnesh, Bagal, Pranay, Ananya, Suman, Utkarsh, Surya, Dinesh, Yatharth, Dayal, Durgesh, Bhavesh, and the loving seniors like Rahul, Palash in the classroom?

Finally, I want to thank my big family - who constantly help me bear the struggle of failures and enjoyment of discovery- for making my life worthwhile.

Abstract

In this thesis, we study the ground-state phases of an extended Bose-Hubbard ladder using the density-matrix renormalization group (DMRG) algorithm. Each chain in the ladder is characterized by an onsite interaction U, nearest-neighbor interaction V, and intrachain hopping J comprising an extended Bose-Hubbard model (EBHM). Though the ground-state phases of a single chain EBHM are well understood, the ladder remains completely unexplored. We assume that the chains in the ladder are coupled through the hopping of atoms in the rungs, and we explore how it affects the current phase diagram of a single chain. We use charged-energy gap, density-wave order, and non-local string order to identify the ground state phases.

Further, we use finite-size scaling to estimate the phase boundaries of the thermodynamic limit. Restricting the analysis to a unit filling factor, we find that a supersolid state emerges in the phase diagram due to the inter-chain hopping. In particular, the supersolid (SS) state is sandwiched between the superfluid (SF) and the density wave (DW). Interestingly, the emergence of SS is accompanied by a reentrant behavior at which the system undergoes SS-DW-SS transition as a function of the contact interaction strength (U). Other states such as Mott-insulator and Haldane insulator may arise depending on the onsite interaction strength or boundary conditions.

We provide a comprehensive picture of the role of inter-chain tunneling on the ground state properties by calculating the superfluid correlation, rung correlation, rung-rung correlation, rung-leg correlation, and entanglement. Further, we show that removing a single rung in the ladder may have drastic effects on the phase diagram. We propose two realistic setups based on dipolar atoms/polar molecules and Rydberg-dressed atoms loaded in optical lattices for implementing the symmetric Bose-Hubbard ladder. Our studies open up various directions in the physics of the Bose-Hubbard ladder. For instance, one can investigate the effect of hopping in a multi-leg ladder or the quantum quench dynamics through the reentrant region, including the Kibble-Zurek mechanism.

Contents

List of Figures

Chapter 1

Introduction

A physical system changes its fundamental properties drastically when it goes from one phase to another via phase transition [1]. Although microscopic thermal fluctuation drives this macroscopic change in a finite temperature system, the thermal fluctuation dies out when the temperature approaches absolute zero. However, in a quantum system, due to the Heisenberg uncertainty relation, quantum fluctuation still exists at $T = 0$, and when these quantum fluctuations are strong enough, it can bring macroscopic change (i.e., phase transition) whereas a classical system cannot do so. These are called "quantum" phase transitions (QPT) [2]. We will see that competition between kinetic and interaction energy is fundamental to the quantum phase transition, which is inherently different from competition between internal energy and entropy, observed in a classical phase transition.

A paradigmatic example of QPT is the Bose-Hubbard model(BHM). In one dimension, where the fluctuations are important, an extension of this model leads to phases like Mott-insulator, superfluid, Haldane insulator, and density waves [3] in the commensurate filling. However, unlike the higher dimension [4], no supersolid is observed in 1D [5]. To understand this issue of dimensionality, we consider a two-leg ladder case and investigate the role of inter-chain tunneling on the ground-state phases of this model, with a certain context to supersolidity. This type of model also can be mapped to spin-model [6] or fermionic systems [7], which allows simultaneous study of different models. On top of that, strong correlations, independent control of interaction parameters, and large bosonic Hilbert space can make this an ideal playground for developing theoretical and experimental ideas on quantum simulators [8, 9].

These kinds of Hubbard ladder have been studied previously with different motivations [6, 10], without any context to supersolid. Nonetheless, these published works help us to explain the results of this thesis. The most general extended BHM in a ladder scheme consists of several parameters, which in the non-homogeneous case and different boundary conditions can produce many new phenomena in principle. However, we only consider a symmetric ladder for simplicity, where the couplings in both legs are the same. We restrict our model to an average density of 1 with an open boundary condition, and we are left with three independent parameters. The interplay of these parameters leads to several ground-state phases, which will be our primary result. We employ a large-scale density-matrix renormalization algorithm [11] in numerical simulation to obtain the ground state. Different correlation functions are calculated to characterize the ground states and understand the specific role of inter-chain tunneling. Due to computational cost, we have kept our DMRG simulation up to a lattice of 80×2, with a maximum number of 6 bosons per site.

In chapter 2, after introducing the Bose-Hubbard model, we discuss its two phases: the Mott-insulator and superfluid. Using a perturbative mean-field theory approach [12], we summarize the phase diagram and its limitations in 1D. Later we introduce the concept of energy-gap, which is used to draw the DMRG phase diagram [13]. In chapter 3, we extend the BHM with the nearest-neighbor repulsive interaction. New phases like density waves, Haldane insulator, and supersolid are characterized with correlation functions [3] and energy gap, which we extensively use for the later part. We also show how the scaling of order parameters and energy gap is done to reach the thermodynamic limit [3, 14]. In the end, we discuss the phase diagrams of 1D extended BHM [3, 15].

Chapter 4 defines the extended Bose-Hubbard ladder [6, 10], what methods and observables we use to draw the phase diagrams, and understand the phases. We also suggest two possible experimental setups to model our Hamiltonian [16, 17]. In Chapter-5, first, we explain the phase diagrams with weak and strong on-site interaction and the effect of inter-chain tunneling in the phases. Then, we show a reentrant phase diagram for fixed inter-chain tunneling and discuss the evidence for reentrance. We also study the effect on entanglement in our model and how the phase diagram changes if we remove one central rung. At last, we show the existence of the Haldane insulator using a different boundary condition [6].

In conclusion, we summarize our results and give an outlook about what we could not address due to time constraints and directions for further research.

Chapter 2

Bose-Hubbard Model

In the context of quantum phase transition [2], the Bose-Hubbard model is much simpler than fermionic systems as the fermionic Mott transition is complicated by the fact that the anti-ferromagnetic transition and localization transition occur at the same point [18]. However, it supports non-trivial phase transitions, which makes it ubiquitous in many-body physics. This model was first introduced in liquid helium to study superfluid to insulator transition [19]. Here, we look at this in a periodic lattice potential, with an average density (ρ) of 1. Dynamics of atomic Bose gas in optical lattice (Appendix.B) can realize the Bose-Hubbard model [20]. Truncating the inter-particle interaction upto two-body terms, the system is described by the many-body Hamiltonian [20] :-

$$H[\hat{\psi}^\dagger,\hat{\psi}] = \int dx\, \hat{\psi}^\dagger(x)\Big(-\frac{\nabla^2}{2m}(x) + V_{lat}(x) - \mu\Big)\hat{\psi}(x) + \frac{1}{2}\int dx \int dx'\, \hat{\psi}^\dagger(x)\hat{\psi}^\dagger(x')V(x-x')\hat{\psi}(x')\hat{\psi}(x) \tag{2.1}$$

where $\hat{\psi}(x)$ is a bosonic field operator for atoms, m is the atomic mass, μ is the chemical potential, $V_{lat}(x)$ being lattice potential and $V(x-x')$ is the 2-body interaction between two atoms at x and x'. Here we consider $\hbar = 1$.

Wannier states: Unlike the continuum case, where the energy eigenstates can be written as Bloch waves: $\phi_k(x)$ [21], in optical lattices, we need to construct unitary superposition of Bloch states to get well-localized functions around the lattice sites for each band n, called as Wannier function : $w_n(x-x_i) = \frac{1}{\sqrt{N}}\sum_k e^{-ikx_i}\phi_k(x)$, which is localized around x_i, decaying exponentially around it (fig.2.1). These functions are orthogonal for different bands n as well as for different sites x_i. Although these single-particle Wannier functions neglect the effect of wave-function broadening in presence of two particle at a site, instead using the two-particle Wannier functions does not show significant effect unless used in precision measurements or metrology [22]. That is why we mostly consider the single-particle Wannier basis, which is mathematically convenient. Now, in this Wannier basis, we can expand the field operators as [23]

$$\hat{\psi}(x) = \sum_i \sum_m \hat{b}_{m,i} w_m(x - x_i) \tag{2.2}$$

where $\hat{b}_{m,i}(\hat{b}^{\dagger}_{m,i})$ annihilates (creates) a boson in the mode represented by $w_m(x-x_i)$ at the i'th site, and satisfy the commutation relation, $[\hat{b}_{m,i}, \hat{b}^{\dagger}_{n,j}] = \delta_{ij}\delta_{mn}$ [24].

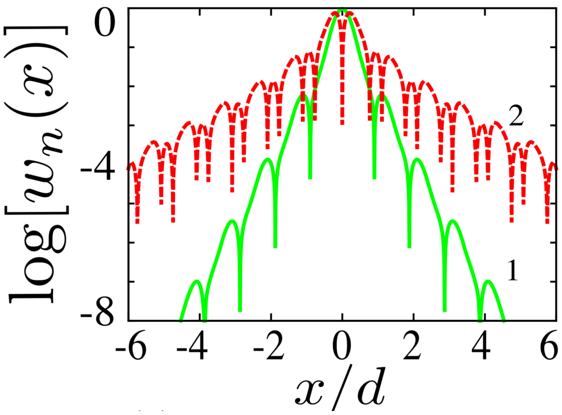

Figure 2.1: Maximally localised Wannier functions for two lowest Bloch bands in a 1D sinusoidal optical lattice. Taken from Ref. [24](Fig.2(a))(Green:band 1, Red: band 2)

Putting (Eq.2.2) in the Hamiltonian (Eq.2.1), we reach to a multiband Bose-Hubbard hamiltonian in second-quantized form-

$$H[\hat{b}^{\dagger}, \hat{b}] = -\sum_{m,n} \sum_{i \neq j} J^{m,n}_{i,j} \hat{b}^{\dagger}_{m,i} \hat{b}_{n,j} + \sum_{m,i} (\varepsilon^m_i - \mu) \hat{b}^{\dagger}_{m,i} \hat{b}_{m,i} + \frac{1}{2} \sum_{m,n,o,p} \sum_{i,j,k,l} U^{mnop}_{ijkl} \hat{b}^{\dagger}_{m,i} \hat{b}^{\dagger}_{n,j} \hat{b}_{o,k} \hat{b}_{p,l} \tag{2.3}$$

where $\hat{b}_i, \hat{b}^{\dagger}_i$ are bosonic annihilation and creation operators with commutation relation $[\hat{b}_i, \hat{b}^{\dagger}_j] = \delta_{ij}$, and the terms have these forms-

$$\begin{aligned}
&(1)\ \text{tunneling:} \quad J^{m,n}_{i,j} = -\int dx \bar{w}_m(x - x_i) \left[-\frac{\nabla^2}{2m} + V_{lat}(x) \right] w_n(x - x_j) \\
&(2)\ \text{energy offset:} \quad \varepsilon^m_i = \int dx \bar{w}_m(x - x_i) \left[-\frac{\nabla^2}{2m} + V_{lat}(x) \right] w_m(x - x_i) \qquad (2.4) \\
&(3)\ \text{interaction:} \quad U^{mnop}_{ijkl} = \int dx \int dx' \bar{w}_m(x - x_i) \bar{w}_n(x' - x_j) V(x - x') w_o(x' - x_k) w_p(x - x_l)
\end{aligned}$$

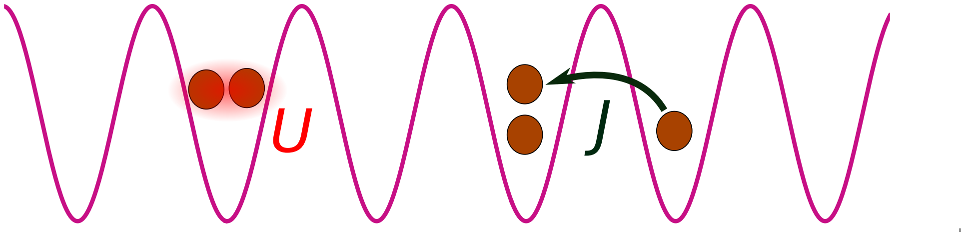

Figure 2.2: Schematic of Bose-Hubbard Model in 1D optical lattice. U defines the onsite repulsive interaction and J defines the nearest-neighbor tunneling

Traditional Bose-Hubbard model: The traditional Bose-Hubbard model [19] is simpler than (eq.2.3) as it assumes many physical situations.

(1) Lowest band: At sufficiently low temperature and small interaction energies, the atoms occupy only the lowest band, i.e., $n = 0$ in this case [23].

(2) Only nearest-neighbor and on-site interaction: For a sufficiently deep lattice, the hopping energy $J_{i,j}$ will be exponentially suppressed for all sites other than the nearest neighbors,i.e., $\sum_{\langle i,j \rangle}$. Similarly, in some practical situations, especially when the system does not have strong long-range force, the on-site interaction term can well-describe the physics, i.e., i=j=k=l in U_{ijkl}. In summary, we have $J_{i,i\pm1}$, ε_i and U_i.

On top of these, for most of the physics problems, we deal with homogeneous systems, and so we can omit suffixes in $J_{\langle i,j \rangle}$, ε_i and U_i. In this case $\varepsilon = const.$, and can be neglected from the Hamiltonian. Now, simply by using the commutation relation and definition of number operator, $\hat{n}_i = \hat{b}_i^\dagger \hat{b}_i$, , we can write $\hat{b}_i^\dagger \hat{b}_i^\dagger \hat{b}_i \hat{b}_i = \hat{n}_i(\hat{n}_i - 1)$. With all these, we will have BHM hamiltonian defined as (also in fig.2.2):

$$H_{BHM} = -J \sum_{\langle i,j \rangle} (\hat{b}_i^\dagger \hat{b}_j + h.c.) - \mu \sum_i \hat{n}_i + \frac{U}{2} \sum_i \hat{n}_i(\hat{n}_i - 1) \tag{2.5}$$

2.1 Phases of Bose-Hubbard Model

Bose-Hubbard model (spin zero) with $U > 0$, exhibits two types of ground-state phases: a superfluid phase and a Mott-insulator phase. Whereas in the superfluid phase, *each* atom is spread out over the entire lattice and exhibiting phase coherence; the Mott-insulator phase has an exact number of localized atoms at individual lattice sites with random phase [25]. To understand these two quantum phases in the grand-canonical model, we define density as,

$$\rho = \frac{\text{Total number of particles}}{\text{Total number of site}} \tag{2.6}$$

2.1.1 When $\rho \in \mathbb{Z}$: Commensurable density

(1) <u>In strong coupling limit i.e</u> $J/U \rightarrow 0$: For $\rho = 1$: In this case, there is, on average, one boson per site. If we observe the Hamiltonian(2.5), it says that one-Boson at a site does not cost any on-site(U) energy. Here, as we consider $U \rightarrow \infty$ and if we want to minimize the energy for the ground state, the on-site interaction should not contribute. So, it must be the case that there is precisely one boson at each site, maintaining no contribution from U in the ground state energy.

For $\rho \geq 2$ ($\rho \in \mathbb{Z}$), we can think of the case as competition between $-J$ and U. The term with J wants to delocalize the atom, but the energy cost for that is U, and thus in $U \gg J$, the hopping process is suppressed.

In summary, for an integer number-density, bosons will be suppressed to move from one-site to another and the system is in an insulating state, called *Mott-insulator* (MI). The many-body ground state of MI can be written as a product of local Fock states at each lattice site [12,18]-

$$|\Psi_{MI}\rangle_{J=0} \propto \prod_{i=1}^{M} (\hat{b}_i^\dagger)^\rho |0\rangle \tag{2.7}$$

where M is the total number of lattice sites, and the filling factor is ρ.

(2) <u>In weak coupling limit i.e</u> $U/J \rightarrow 0$: From the above discussion it is obvious now that when J is strong, tunneling is more favoured. In this limit, the single-particle wave-functions of N atoms spread out over the entire lattice of M sites to minimize the ground-state energy [25]. This quantum state of delocalized bosons is called *superfluid* (SF). The wave-function of SF is given by [18,25]-

$$|\Psi_{SF}\rangle_{U=0} \propto \left(\sum_{i=1}^{M} \hat{b}_i^\dagger\right)^N |0\rangle \tag{2.8}$$

Thus, as the J/U ratio increases, we expect a phase transition from MI to SF state.

2.1.2 When $\rho \notin \mathbb{Z}$: Incommensurable density

In this case, we cannot have a Mott-insulator because that requires an equal and integer number of particles at each site, which is not possible when $\rho \notin \mathbb{Z}$. Consider $\rho = n_0 + \delta n$ where $n_0 \in \mathbb{Z}$. Then these excess bosons (δn) move through the whole system, creating a SF state even for $J/U \to 0$.

Here, we should emphasize that quantum fluctuation plays an essential role in the phase transition. Due to strong fluctuation in atom number, atoms in SF are delocalized and exhibit long-range phase coherence and interference pattern, coming from number-phase uncertainty. Contrary to that, atom-number fluctuation is reduced in the MI phase, leading to the increasing fluctuation in the phase, for which it loses phase coherence. In this way, using the quantum uncertainty principle, we explain how coherence is lost in MI, but present in SF.

2.2 Phase Diagram of BHM

The Bose-Hubbard model is one of the most straightforward many-body systems that cannot be reduced to a single-particle Hamiltonian [12], and the challenge for an analytical solution comes from the tunneling term in the eq.2.5.

2.2.1 Perturbative Mean-Field theory

In perturbative mean-field theory (MFT), we neglect second order fluctuations as $(\hat{b}_i^\dagger - \langle \hat{b}_i^\dagger \rangle)(\hat{b}_j - \langle \hat{b}_j \rangle \simeq 0$, and define order parameter, $\varphi \equiv \langle \hat{b} \rangle$. This reduces the tunneling term as local terms -

$$\Rightarrow \hat{b}_i^\dagger \hat{b}_j \simeq \varphi \hat{b}_j + \varphi \hat{b}_i^\dagger - |\varphi|^2 \tag{2.9}$$

Now, if we use perturbation in J/U, we can obtain free energy as, [12]-

$$E(\varphi, \bar{\varphi}) = \underbrace{\frac{U}{2}\rho(\rho-1) - \mu\rho}_{\equiv a_0} + \underbrace{Jz|\varphi|^2 + \left[(Jz)^2\left(\frac{\rho+1}{\mu - U\rho} + \frac{\rho}{U(\rho-1)-\mu}\right)\right]|\varphi|^2}_{\equiv a_2|\varphi|^2} + a_4|\varphi|^4 + \mathcal{O}(|\varphi|^6) \tag{2.10}$$

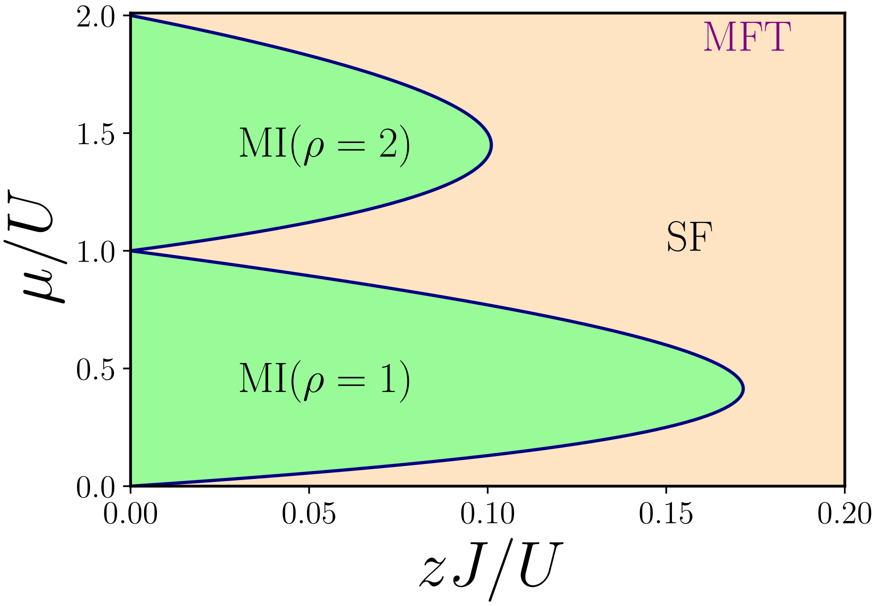

Figure 2.3: MFT phase diagram for BHM in (μ, J) plane, where Mott lobes of $\rho = 1$ and 2 are surrounded by SF. Solid lines show MI-SF transition. (MI:Mott-insulator ; SF:superfluid)

where z is the coordination number. In Landau's phase transition theory, by minimizing this energy potential $E(\varphi, \bar{\varphi})$ with respect to φ, we can show that the MI-SF transition line is defined by

$$a_2 = Jz + (Jz)^2 \left(\frac{\rho + 1}{\mu - U\rho} + \frac{\rho}{U(\rho - 1) - \mu} \right) = 0 \tag{2.11}$$

plotted in (fig.2.3). We can see that MI lobes of $\rho = 1, 2$ are surrounded by SF phase. Looking at that phase diagram, we can conclude that SF exists for all $J > 0$, depending on μ, even when $U/J \gg 1$. There are always two critical points (μ_c) for MI-SF transition at any J/U value, other than the tip of the lobe. These are called μ_+ and μ_- corresponding to the upper and lower critical line, which defines the commensurate-incommensurate transition via adding or removing one particle. (sec.2.1.2). Thus we can identify

$$\mu_+ = E^0(N+1) - E^0(N); \quad \mu_- = E^0(N) - E^0(N-1) \tag{2.12}$$

where $E^0(N)$ is the ground-state energy for the system of N Bosons. $\mu_+(\mu_-)$ are particle (hole) excitation gap, quantifying the energy cost (gain) to add (remove) a particle from the system.

In this (μ, J) plane, we can see the signature of *two different types* of MI-SF transition as discussed in sec.2.1. On the sides of the Mott-lobe, where $\mu_+ \neq \mu_-$, the phase transition is driven by *density* fluctuations [19]. However, on the constant density line ($\mu_+ = \mu_-$), it is driven by *phase* fluctuation, depending on the strength of J/U, defined by the tip of the lobe. In case of 1D, the coordination number is $z = 2$ and the tip of the $\rho = 1$ MI lobe is at [23],

$$\left(\frac{J}{U}\right)_c \simeq 0.08578. \tag{2.13}$$

This tip also signifies the critical point J_c, after which all points are in the SF phase. In the thesis, we have worked with commensurate $\rho = 1$, which means whenever we say MI-SF transition, it means tip-of-the-lobe point.

BHM in 1D: In low- dimensional, e.g.,- 1D or quasi-1D systems, the fact that two particles cannot cross without feeling their interaction makes slight quantum fluctuation very important [26–28], leading to novel physics. On the other hand, technological revolutions are towards miniature objects, for which studying phases in low-dimension is instrumental. However, the mean-field theory fails in 1D and quasi-1D, as it neglects the critical quantum fluctuation of the system. Hence, we will be using the best approximate numerical method available for such purpose; namely, density-matrix renormalization group algorithm(DMRG) [29] (Appendix.A).

2.2.2 Charged Energy Gap

Obtaining the critical point at constant density means getting the tip of the lobe, i.e., when $\mu_+ = \mu_-$. For that purpose, we can define a quantity called charged energy gap as [30–33]

$$\Delta_L^c = \mu_+(L) - \mu_-(L) = E_L^0(N+1) + E_L^0(N-1) - 2E_L^0(N) \tag{2.14}$$

such that when $\Delta_L^c = 0$, we have a phase transition from MI to SF. Here, L defines the system size. Previously, in the mean field theory (eq. 2.12), we do not have L- dependence as the energy functional there depends on the coordination number z, and that means it is already with infinite or periodic lattice. The ‘charge’ in the charged energy gap denotes the number of particles, that is, the charged gap is the energy gap involving the number of particles. On top of our understanding from the MFT phase diagram, if we add this definition, it is clear that MI should be gapped phase as in Mott lobe $\mu_+ \neq \mu_- \Rightarrow \Delta^c \neq 0$, whereas SF should be gapless.

However, this charged gap directly defines superfluidity without any context of the MFT phase diagram. For that, consider a 1D lattice with a filling factor =1, where there is exactly one particle per site (fig.2.4). Let us say the energy of this configuration is $E_L^0(N)$. Now, if a particle tunnel from one site to another, (as shown in the fig) the new configurations can be thought of as creating one extra-particle at one site, whereas removing another particle at another site, which costs the energy -

$$[E_L^0(N+1) - E_L^0(N)] + [E_L^0(N-1) - E_L^0(N)] \tag{2.15}$$

which is the same as Δ_L^c. This implies that the charged energy gap quantifies the energy cost to move a particle on a lattice, i.e., the delocalization of particle-hole excitation throughout the lattice. So, a gapless phase means it does not need any energy for moving particles, which is the case in SF. On the other hand, gapped phases should be insulated, as particles need extra energy to move around. From this discussion of the charged energy gap, it should be clear that the charged energy gap is a robust probe to identify gapped to gapless transitions, e.g., MI to SF transition.

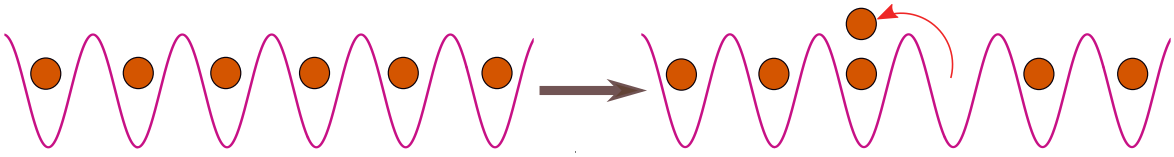

Figure 2.4: Explaining charged energy gap as the energy needed to move a particle in the lattice

2.2.3 DMRG Phase diagram for 1D BHM

DMRG algorithm (Appendix.A) is a powerful numerical method to obtain ground-state energy of an extensive 1D system, which is otherwise impossible using exact diagonalization due to the large Hilbert-space dimension. We need to work with large lattices to get rid of finite-size effects, and crucial in strongly correlated systems as quantum phase transitions occur only in the thermodynamic limit (large-L) at zero-temperature [12].

Here, we obtain a similar phase diagram (like fig.2.3) for BHM by calculating $\mu_\pm$, but now using finite-size scaling of DMRG results. Although finitely many bosons can occupy each lattice site in principle, in this DMRG calculation, we have restricted it to $n_{max} = 4$ for computational cost, which turns out to be good [14]. By calculating $E_L^0(N), E_L^0(N+1), E_L^0(N-1)$, we have obtained $\mu_\pm(L)$ for $L = 80, 100, 120, 200$. For these calculations, we have gone till bond-dimension of $\chi = 400$, with maximum 20 sweep (Appendix.A). Then by extrapolating the results of these finite-size lattices with respect to $1/L$, the thermodynamic limit is obtained (fig.2.5). These $\mu_\pm$, for different J/U, give us the DMRG phase diagram(fig.2.6) in the $(\mu/U, J/U)$ plane. As we can see, this phase diagram is drastically different from the MFT phase diagram (fig.2.3). The tip of the lobe is at $(J/U)c = 0.277$ [13], which is far from the MFT value (eq.2.13).

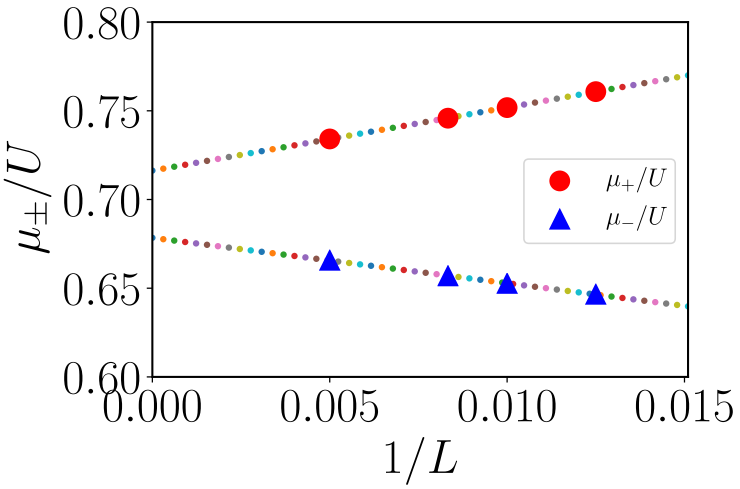

Figure 2.5: Scaling of particle and hole excitation gap with 1/L ($\rho = 1, J = 1, U = 4$). Here $\mu_+ = 0.716 + 3.555/L$ and $\mu_- = 0.678 - 2.559/L$.

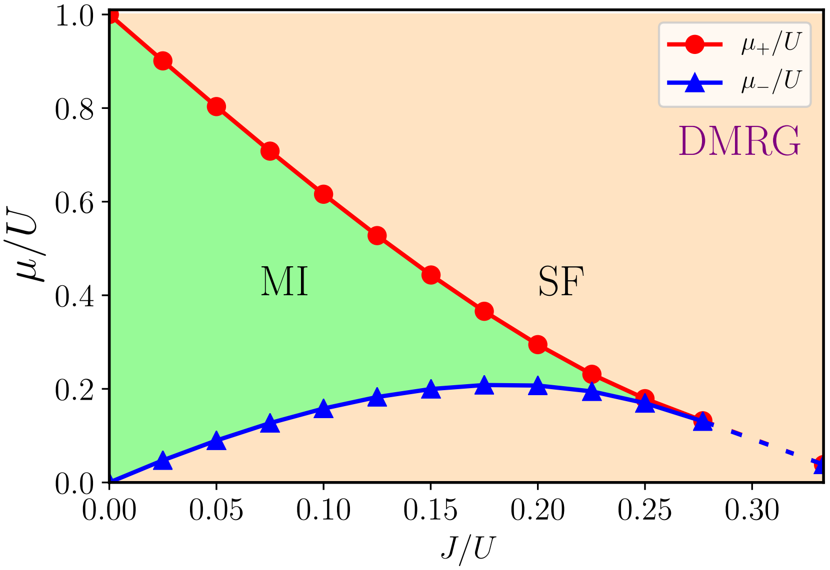

Figure 2.6: DMRG phase diagram of BHM for $\rho = 1$. The dashed line indicates region with integer density. Reentrance from MI-SF-MI is observed around $J/U \simeq 0.22$ (MI:Mott-insulator, SF:superfluid)

In this 1D case, the correlation function in SF phase decays algebraically rather than having a long-range order, and that is why the phase is called quasi-SF, instead of true-SF. For constant integer filling, the SF-MI transition (at the tip) is of the Berezinskii-Kosterlitz-Thouless (BKT) type [13, 31], and the existence of this BKT transition in 1D BHM can be explained by the scaling theory discussed in Fisher *et al.* [19], which showed that for a d-dimensional BHM, phase transition in constant density line (tip) is in the same universality class of $(d+1)$-dimensional classical XY-model. Hence, 1D-BHM corresponds to the 2D-XY model, and it has a BKT transition [34].

Reentrance: In the DMRG phase diagram (fig.2.6), we can see that for $J/U > 0.2$, the lower phase boundary is bending down [13], which means MI is reentrant as a function of J/U. The reentrance is very non-trivial because this means that with increasing kinetic energy, the system localizes. MFT fails to capture these as perturbative series of J/U is incorrect for large J/U values. Particle-hole asymmetry in Mott-lobe, along with BKT-transition is considered responsible for this reentrance [18]. In higher dimensions,$(d \geq 2)$, this reentrant behavior is missing as those transitions are not of BKT-type. Also, for a higher filling factor, the kinetic energy is higher due to more bosons, and the tip of the lobe shrinks to a smaller J/U value, leaving no chance of reentrance behavior to appear [35].

Chapter 3

Extended Bose-Hubbard Model

Quantum gases are mostly governed by the 2-body interaction between particles [12]. In the previous chapter, we discussed bosons with short-range interaction U. However, in the last two decades, it is found that dipolar interactions between a pair of magnetic or electric dipoles [36–38] can lead to novel phases of matter in a strongly correlated regime. The dipole-dipole interaction being *long-range* and *anisotropic*, is quite different than isotropic, short-range contact interaction [38]. Simultaneously, the experimental possibilities to cool and trap polar molecules and atomic species with a larger magnetic moment make dipolar gas a topic of huge attraction [39].

With this motivation, we can add a nearest-neighbor interaction term, at minimum, to the BHM to account for the long-range interaction. For simplicity, we consider this as constant over the lattice. This extended Bose-Hubbard model (EBHM) (fig.3.1) hamiltonian then written as-

$$H_{EBHM} = -J \sum_{\langle i,j \rangle} (\hat{b}_i^\dagger \hat{b}_j + h.c.) - \mu \sum_i \hat{n}_i + \frac{U}{2} \sum_i \hat{n}_i(\hat{n}_i - 1) + V \sum_i \hat{n}_i \hat{n}_{i+1} \tag{3.1}$$

where J, U, μ have their usual meaning as in BHM and V defines the nearest-neighbor repulsive interaction.

Mapping to Heisenberg spin-S model: In strong U limit, EBHM can be mapped to anisotropic Heisenberg spin-S chain [7, 32, 40] using the Holstein-Primakoff transformation

$$\begin{aligned} S_i^+ &= \sqrt{(2S - n_i)}\, b_i \\ S_i^- &= b_i^\dagger \sqrt{(2S - n_i)} \end{aligned} \tag{3.2}$$

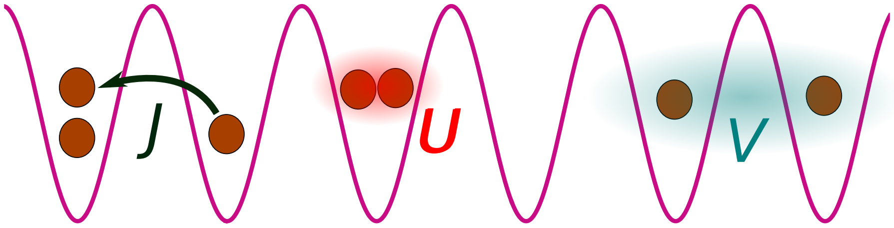

Figure 3.1: Schematic of extended Bose-Hubbard model in a 1D optical lattice. J provides tunneling to nearest-neighbor, U and V are respectively on-site and nearest-neighbor interaction.

$$S_i^z = S - n_i$$

and the spin hamiltonian has the form -

$$H = \sum_i \left[2J(S_i^x S_{i+1}^x + S_i^y S_{i+1}^y) + SVS_i^z S_{i+1}^z + \frac{SU}{2}(S_i^z)^2 \right] \tag{3.3}$$

Assuming, $\langle S_z \rangle = 0$ (i.e., $\rho = \langle n_i \rangle = S$), this mapping is most correct if the fluctuation is small $\delta n_i = n_i - S \ll S$ and the maximal site occupation $n_{max} \leq 2S$. In our case, $\rho = 1$, which implies $S = 1$, meaning we need $n_{max} \leq 2$ for accurate mapping. This is not the case for small U, and that is why this mapping can show a significant departure from the correct results in small U.

3.1 Phases of extended Bose-Hubbard model

This section discusses how different phases arise due to competition between the Hamiltonian terms and how to characterize those. In the small V region, this model is the same as BHM, and we have the usual MI and SF phases. The new phases emerge in large V in a strongly correlated regime. Here, we have restricted discussion to the 1D system only, with $\rho = 1$ and $U, V > 0$. By fixing ρ, we fix total N for a fixed lattice size, and hence μ is also constant. We set the energy scale by $J = 1$, which is the same as saying the parameters scale as U/J and V/J.

3.1.1 When J is small

J being small, we mean the system has large U and V. Here, we can have three extreme situations considering U and V, namely $U \gg V$, $U \simeq V$, $U \ll V$.

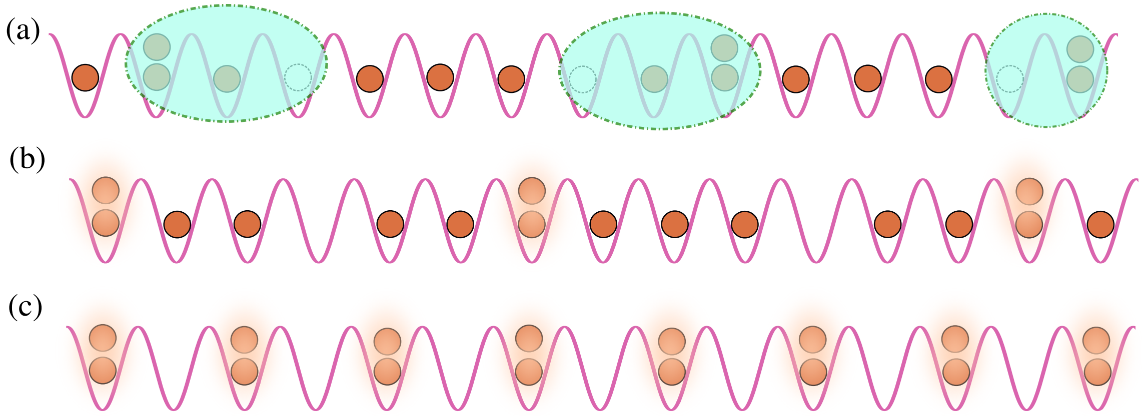

Figure 3.2: Insulating phases of 1D EBHM for $\rho = 1$: (a) Bound particle-hole pairs in MI, (b) Alternating particle-hole pairs (like DW) separated by string of non-zero fluctuating sites (a bunch of 0's) in HI, (c) Density wave pattern of (....2-0-2-0-2...) in DW phase (MI:Mott insulator, HI: Haldane insulator, DW: density wave)

(1) When $U \gg V$: V being negligible, we get back to the usual BHM. On top of that, we have a small J, which implies the system will be in the **Mott-insulator** phase, characterized by a non-zero charged gap and fixed number of particles at each lattice site. To mention, due to quantum fluctuation, there can be *bound* particle-hole pairs in MI (fig.3.2(a)), quantified by a non-local order parameter called parity correlation function [6, 41]-

$$\mathscr{O}_P(j,r) \equiv \left\langle \exp\left\{ i\pi \sum_{j<k<j+r} \delta\hat{n}_k \right\} \right\rangle \tag{3.4}$$

(2) When $U \ll V$: In a strong V regime, the system wants to minimize the term $\hat{n}_i\hat{n}_{i+1}$. We cannot have a homogeneous MI-like structure as it costs energy $\sim V$ for each pair of lattice sites. In fact, a new wave-like pattern of ....$2-0-2-0-2-0$.... emerges, which can minimize the interaction (fig.3.2(c)). This is called **density wave** (DW). This DW-order is characterized by a density-fluctuation correlation function [3]-

$$\mathscr{O}_{DW}(j,r) \equiv (-1)^r \langle \delta\hat{n}_j \delta\hat{n}_{j+r} \rangle \tag{3.5}$$

where $\delta\hat{n}_j = \hat{n}_j - 1$. On top of this, as J is small, the system does not delocalize, and it is a gapped insulator phase.

(3) When U $\simeq V$: In this regime, there is a possibility of a new gapped insulating phase [42], which is neither MI nor DW. Like Haldane gapped phase [43] of quantum spin-1 chain, this new phase is identified only by a highly nonlocal string correlation function [6,41,42]-

$$\mathscr{O}_{string}(j,r) \equiv \left\langle \delta\hat{n}_j \exp\left\{ i\pi \sum_{j\leq k<j+r} \delta\hat{n}_k \right\} \delta\hat{n}_{j+r} \right\rangle \tag{3.6}$$

By analogy to spin-system, it is called bosonic **Haldane insulator** (HI). It has alternating particle-hole pairs separated by a string of non-zero fluctuating sites (fig.3.2(b)). We can think that HI arises as a compromise between moderate U/J, which wants to delocalize the particle-hole pairs, and moderate V/J, which wants particle-hole pairs to be neighbors [6].

Originally, Dalla *et al.* [42] considered large U, such that local Hilbert space can be truncated at 3 occupation states $n = 0,1,2$ for $\rho = 1$ case, which can be mapped to an effective spin-1 model with $S_i^z = n_i - \rho$ as (eq.3.3),

$$H' \simeq J\sum_i (S_i^+ S_{i+1}^- + h.c.) + \frac{U}{2}\sum_i (S_i^z)^2 + V\sum_i S_i^z S_{i+1}^z \tag{3.7}$$

In this spin-1 language, DW corresponds to the anti-ferromagnetic(AF) order of the spin along z-direction, whereas MI looks like $S_i^z = 0$ state for each site, with bound particle-hole excitation of $S_i^z = \pm 1$. HI phase although mostly contain sites with $S_i^z = 0$, it has unusual ordering. The spin-HI is identified with *fully* broken hidden $Z_2 \times Z_2$ symmetry [44]. That can be revealed by introducing a non-local unitary transformation, which makes string-order parameter of the spin-1 hamiltonian H' to ferromagnetic order of another Hamiltonian $\tilde{H}'$. With this, it was shown that in HI regime, ferromagnetic order for both x and z direction are non-zero, implying $Z_2 \times Z_2$ symmetry breaking [44], and there are 4-degenerate ground-states of $\tilde{H}'$. However, the original H' has a unique ground state with near degeneracy. From the original Hamiltonian's perspective (eq.3.1), it seems this $Z_2 \times Z_2$ symmetry of $\tilde{H}'$ is connected to $U(1)$ symmetry of H.

3.1.2 When J is large

In a large-J limit, the kinetic energy of the system is more, and the system wants to delocalize.

(1) When $U \gg V$: V being negligible, the model has **superfluid** phase like BHM in the strong-J limit, characterized by $\Delta^c = 0$, and the SF-correlation function, defined as [13]-

$$\Gamma(j,r) = \langle \hat{b}_j^\dagger \hat{b}_{j+r} \rangle \tag{3.8}$$

which decays as $\Gamma_{SF}(r) \propto \frac{1}{r^K}$ in SF. Using the analogy of Luttinger liquid [45], the exponent at BKT transition is expected to be $K_c = 1/4$, and by a DMRG calculation, it is being verified [13].

(2) When $U \ll V$: As we discussed previously (sec.3.1.1), in a strong V regime, there will be a DW-order. However, strong J can prevent the insulating behavior of the system by gaining superfluidity and diminishes the DW-order [13], especially in 1D. There is also another possible phase that can support both the DW-order and superfluidity. This new phase is called **supersolid** (SS) [46]. Although this simultaneous presence of density-order and superfluidity is unusual, it is useful to think that the entire or part of the modulated solid structure is moving together in SS [47].

Below in this table 3.1, we have summarised minimal characteristics for the phases discussed in this section [5]. The insulators such as MI, HI, and DW are gapped, and SF and SS are gapless. The density order is characterized by $\mathcal{O}_{DW}$, which is non-zero in DW and SS. Non-zero $\mathcal{O}_{string}$ characterizes the HI; however, DW also has a non-zero value of that because $\mathcal{O}_{string}$ contains the part of $\mathcal{O}_{DW}$ (eq.3.6).

Table 3.1: Order parameters to characterize phases

Phases	Δ^c	$\mathcal{O}_{DW}$	$\mathcal{O}_{string}$
MI	$\neq 0$	$= 0$	$= 0$
SF	$= 0$	$= 0$	$= 0$
HI	$\neq 0$	$= 0$	$\neq 0$
DW	$\neq 0$	$\neq 0$	$\neq 0$
SS	$= 0$	$\neq 0$	$\neq 0$

3.2 Phase diagram of EBHM

Using the table. 3.1, in this section, we discuss the phase diagram of 1D-EBHM for fixed $\rho = 1$, obtained by DMRG [3] in open-boundary condition (OBC). We choose OBC, as DMRG works efficiently there [48]. The main challenge to obtain the phase transition points comes from the finite-size effect [12], and to solve that, scaling of order parameters is needed. Here, we first demonstrate how the phase transition points are obtained using scaling, and the example presented here will also show that we can have the wrong conclusion without scaling.

3.2.1 Scaling of order parameters

For a fixed lattice size, we calculate the order parameters and correlation functions in the central bulk (L/2 sites) part only, discarding the $L/4$ sites at both ends to reduce the edge-effect. To remove the initial-position (j) dependence of the order parameters, it is averaged over all possible initial sites (j) inside the bulk for a fixed r, i.e.,

$$\mathscr{O}(r) = \frac{1}{N_r} \sum_{j \in M} \mathscr{O}(j,r) \tag{3.9}$$

where M defines the bulk of the lattice and N_r is the total number of possible segments of length r inside M. Then from the plot of $\mathscr{O}(r)$ vs r (fig.3.3(a)), we obtained the $r \to \infty$ limit of the order parameters. However, this still contains the effect of the lattice size L (fig.3.3(b)). To remove that, we can extrapolate finite lattices' $\mathscr{O}$ to thermodynamic limit, if we need that value. However, here we are interested in obtaining the critical point, not the $\mathscr{O}$ at $L \to \infty$. For that, first, we get the phase transition point for finite lattices by identifying where $\mathscr{O}(r \to \infty)$ starts having non-zero value, and then extrapolate those (finite-size) transition points with $1/L$, to finally get the critical point at the thermodynamic limit (fig.3.3(b-inset)).

Example ($\mathscr{O}_{DW}$): As shown in (fig.3.3)(a), averaged $\mathscr{O}_{DW}(r)$ decays with r to a constant value in large r limit, which is considered as the $(r \to \infty)$ value. Then in fig.3.3(b), we can see the L-dependence, as for smaller L, DW-order emerges at smaller V. We consider $\mathscr{O}_{DW} \geq 0.01$ as non-zero, below this are considered zero. V_{min} is defined as the critical point when $\mathscr{O}_{DW}$=0.01. By fitting three different V_{min}'s of $L = 50, 100, 150$, linearly with $1/L$, we get V_c for $L \to \infty$, which is the y-intercept in fig.3.3(b)(inset). Here, we get $V_c \simeq 3.026 \pm 0.02$, where the uncertainly comes from the least count of our data, which is 0.02.

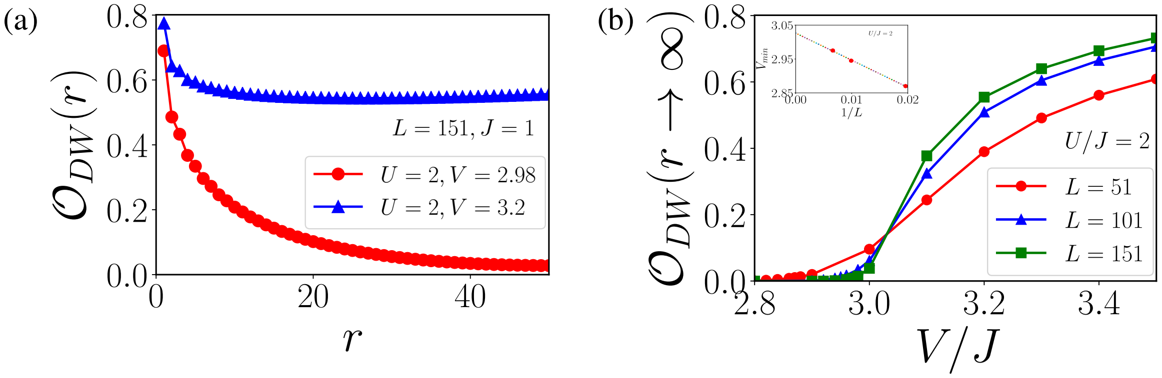

Figure 3.3: Finite-size scaling of DW-order parameter to obtain critical point V_c: **(a)** Density-wave order parameters ($\mathcal{O}_{DW}$) as a function of distance r for V=2.98 and V=3.2 in a lattice of L=151 with U/J=2 **(b)** Extrapolated density-wave order parameters ($\mathcal{O}_{DW}(r \to \infty)$) as a function of V for different lengths L. For example, in L=51, the system exhibits a transition to DW at V=2.87 ± 0.02, where the $\mathcal{O}_{DW}$ starts being finite(0.01) . **Inset**: Linear fit of transition point (V_{min}) in finite-size lattice with $1/L$ to obtain the thermodynamic critical point. Here $V_{min} = 3.026 - 8/L$, meaning $V_c = 3.026$

3.2.2 Scaling of energy gap:

As most critical points are gapless, the energy gap serves as an excellent quantity to obtain a phase diagram. Also, in DMRG, we minimize energy to get the ground state, so energy has the slightest numerical error. On the other hand, calculating any order parameters and correlation functions involves several steps, owing to more truncation and numerical error [29]. Unfortunately, in a finite system, the gap is non-zero even at critical points, which challenges identifying those critical points. Here, we discuss two methods for scaling the energy gap and identifying gapless points.

Method 1: In this method, we don't scale the gap to obtain $\Delta^c_{L\to\infty}$. Instead, we get the parameter value where the local minima of the energy-gap is obtained for different L's, and scale those parameter values with respect to $\sim 1/L$ to obtain the critical point in $L \to \infty$ [3, 49]. In (fig.3.4(a)), we show an example, where we obtain $V_{min} = 3.033 - 7.615/L$, implying $V_c \simeq 3.033 \pm 0.02$.

Method 2: This method depends on the scaling theory at critical points [1]. We know that at a critical point, the energy gap follows this relation [10, 14]-

$$\Delta^c_L \sim \frac{1}{L} f\left(\frac{L}{\xi}\right) \tag{3.10}$$

where ξ is the correlation length and $f(x)$ is a scaling function, which follows $f(x) \sim x$ at $x \to 0$. Now, in the gapless points, $\xi \to \infty$, making $f(L/\xi) \sim 0$, and $L\Delta_L^c =$ constant for all L. That means $L\Delta_L^c$ for different L intersect at the critical point [10, 14]. However, due to numerical tolerance, in literature [10], a finite difference between $L_1\Delta_{L_1}^c$ and $L_2\Delta_{L_2}^c$ is also considered as zero. In our calculation, that tolerance value is 0.04, which means if $L_2 - L_1 = 10$, then $L_2\Delta_{L_2}^c - L_1\Delta_{L_1}^c \leq 0.04$ is considered critical. For gapped to the gapless phase transition, $L\Delta_L^c$ curves not only intersect but coalesces and we find a real zero difference between two curves [14]. However, we stick to numerical tolerance of 0.04. We have also observed that changing the tolerance does not affect the qualitative phase diagrams. As an example, in (fig.3.4(b)), we can see how the lines coalesce around or before $V \simeq 3.05$, signifying the phase before that value as a gapless phase. Considering the tolerance limit of 0.04, we obtain $V_c \simeq 3.05 \pm 0.02$, which is inside the error bar of obtained value using method-1.

The example discussed in (fig.3.3,3.4) also proves that although the system is in a strong J/U regime, with a strong V, it does not have a SS phase, as we see that V_c for the destruction of SF and onset of DW coincide. In other words, there is a *direct* transition from SF to DW phase at $V_c \simeq 3.04 \pm 0.02$, and it hints to us the importance of finite-size scaling to obtain critical points, without which someone may claim that SS exists in 1D.

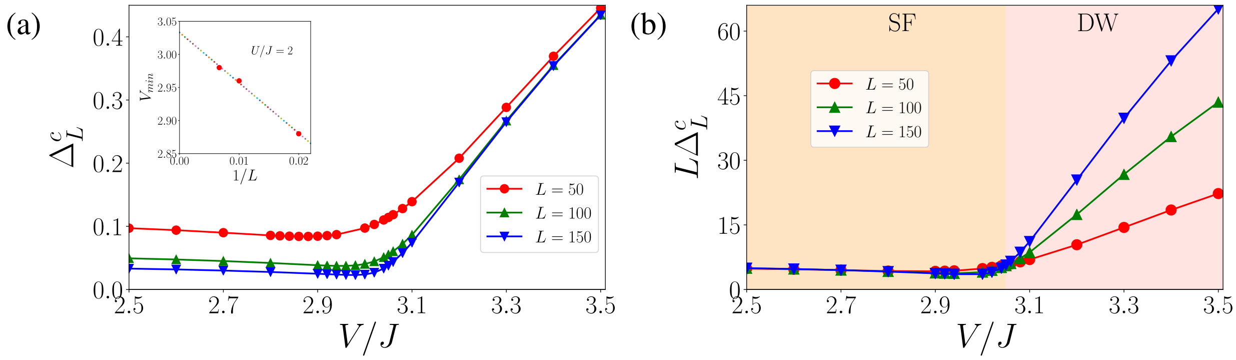

Figure 3.4: Finite-size scaling of the charged gap to obtain critical point V_c: **(a)** Using method 1: Δ_L^c with V for three different L. (**Inset:** Minima of Δ_L^c for different L are linearly fitted to $1/L$ to obtain V_c) **(b)** Using method 2: $L\Delta_L^c$ for different L coalesces at V_c=3.04

3.2.3 Effect of even and odd L

For finite-lattice, in particular to EBHM, the even and odd lattices have different features and challenges. Here we discuss how we can handle those.

Close chain: For periodic boundary condition, if we consider even L, there is two degenerate DW possible, i.e., $|202020\rangle$ and $|020202\rangle$, whereas, for odd L, the DW will get an artificial center (look below at open chain) because, in $|20202\rangle$, the first and last sites also repel and this configuration cannot be stable. We can apply positive and negative chemical potential μ at two ends to lift the degeneracy in even-L [3, 42].

Open chain: As the edge sites have one less neighbor in an open chain than bulk sites, the system always tries to put the maximum number of particles at the edge, minimizing energy cost due to V. In this way, there is no possibility of O's (zero number-state) at the edges and thus no degeneracy in DW. However, this creates a problem for even L. As there must be 2's at the edges, it has to create an artificial node [50] in the middle, like $|2020\rangle|0202\rangle$, which in turn makes a problem for calculating $\mathscr{O}_{DW}$ in the bulk [41]. On the other hand, for odd L, it can have $|2020\rangle|1\rangle|0202\rangle$, without destroying the density-wave structure in bulk. The middle $|1\rangle$ owes to the fact that we have $N = L$, and already two ends are occupied with 2's. As a caution, these classical occupancies should not be taken seriously, as when we calculate local expectation value$\langle\hat{n}_i\rangle$, due to the probabilistic nature of quantum mechanics and numerical calculation, we do not get integer values. As shown later, we get uniform density waves without identifying the middle site in the odd chain.

On the other hand, this $|1\rangle$ in the middle gives the challenge to calculate Δ^c in DW, for $L =$odd, in strong V, low U regime. There the system mainly wants to minimize the nearest-neighbor interaction. While calculating Δ^c_L, when we add or remove one extra particle to $|2020\rangle|1\rangle|0202\rangle$, it can sit in the middle almost without any energy cost giving rise to a gapless phase and can fool us. In other words, $|1\rangle$ can move around the lattice almost at no cost. So, the charged gap is not a good probe here. That is why the charged gap in this regime is calculated for L=even, and DW-order is calculated in L=odd to avoid the problems rising from OBC [51]. However, as we do finite-size scaling, using odd-even does not affect our phase diagram. The above example (fig.3.3,3.4) demonstrates how Δ^c and $\mathscr{O}_{DW}$ gives rise to the same critical point, despite being calculated for even and odd Ls. We do not use opposite μ, as we want to stick with normal boundary conditions and different boundary conditions should be treated separately [15].

3.2.4 Quenching edge-state for HI

The challenge in investigating bulk properties of HI with open boundary conditions is that the result is affected by edge states [52]. There are mainly three ways to handle this problem.

Method 1: Instead of using $N = L$ bosons in the lattice, we can add one extra Boson ($N = L + 1$) for each chain, which results to the magnetization of $\sum_i S_i^z = -1$ in spin-1 language. Due to the Haldane gap, this extra spin is accommodated at the edges, making $S_1^z = S_L^z = 1/2$, without any energy cost, and polarizes the edge states [15, 40, 41]. Although $N = L + 1$ means $\rho \neq 1$, in thermodynamic limit, $\rho \to 1$. Also adding one particle to $\rho = 1$ doesn't change the DW-structure, whereas it can create solitons for $\rho = 1/2$ [53].

Method 2: Applying opposite chemical potentials at the left and right edge sites, we can break the degeneracy of the edge states [6, 15, 41, 42].

Method 3: We can add hard-core bosons at each chain boundary (sites 0 and L+1), lifting the degeneracy [40].

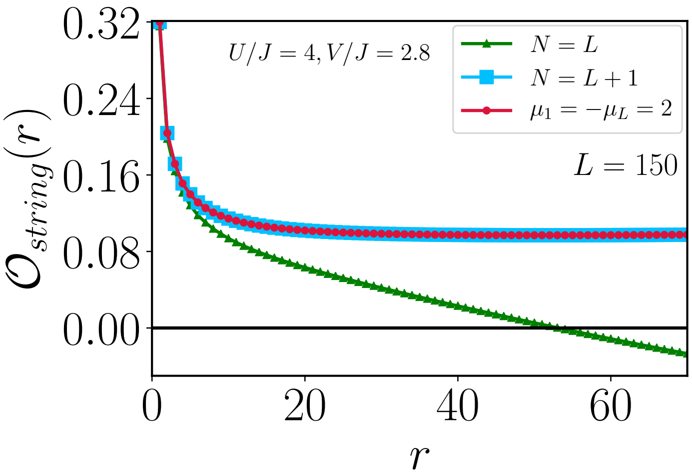

Figure 3.5: Non-zero string order after quenching edge mode in HI: for N=L (without quench), due to edge mode $\mathcal{O}_{string}$ decays to negative value; by adding extra particle (N=L+1) or by applying opposite $\mu_\pm$ at the edge, $\mathcal{O}_{string}$ fixes to a non-zero value

In (fig.3.5), we show how using method-1 and method-2, we can quench the edge states, which in turn change the constantly decaying $\mathcal{O}_{string}$ of $N = L$ case to non-zero string-order.

3.2.5 Phase diagram

In this last section of EBHM, we discuss the phase diagram of 1D EBHM in the $(U/J, V/J)$ plane, obtained by Rossini *et al.* [3] and Kurdestany *et al.* [15]. We can see in (fig.3.6), for both cases,

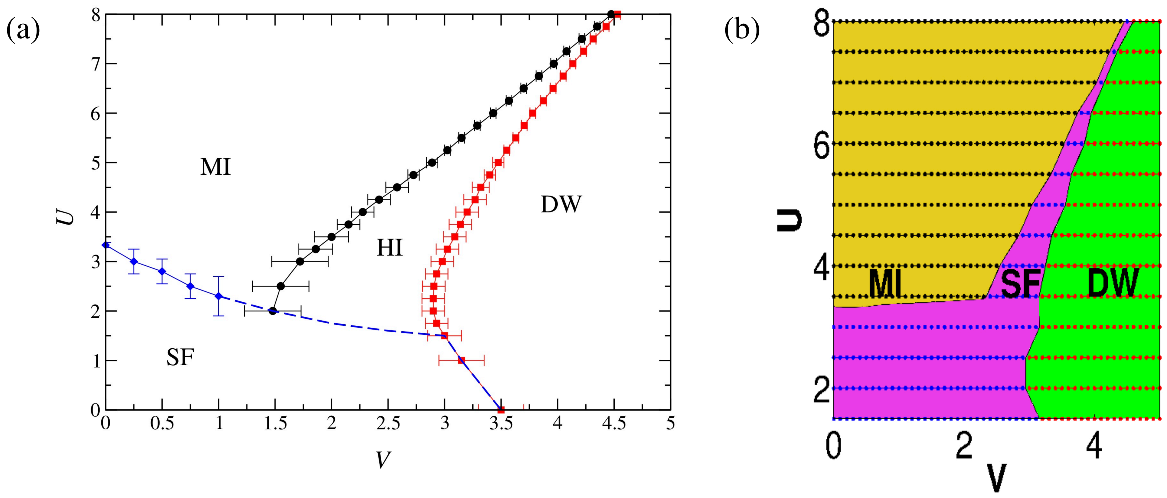

Figure 3.6: Phase diagram in (U,V) plane for 1D EBHM for $\rho = 1$ with $J = 1$: **(a)** $\mu_{\pm}$ applied at the edge: MI, SF, HI, DW are observed (taken from Ref. [3]), **(b)** Without applying any $\mu_{\pm}$: MI, SF, DW observed, HI is replaced by SF (taken from Ref. [15])

without quenching the edge mode [fig-b] and with quenching it using opposite μ [fig-a], MI is observed for large U with small V region, as we discussed in section-3.1. On the other hand, with a strong V, the system is in the DW phase for the same U. For smaller U, where J/U is strong, the SF phase is observed. All these phases are characterized following table.3.1.

Two boundary conditions differ for obtaining the HI phase due to the spurious effect of edge states. In the presence of gapless edge mode, for $N = L$ case (fig-b), we observe the SF phase in place of the HI phase, whereas by quenching it in (fig-a), we find the HI phase in the $U \simeq V$ regime.

Existence of supersolid: While in the above phase diagrams we cannot see SS, its possible existence is shown in [15, 40], where the authors are also doubtful. In 2D, with commensurate fillings, it is present [54, 55]. With incommensurate filling above $\rho = \frac{1}{2}$, SS phase appears in both 1D [56, 57] and 2D [4]. Only unusual thing is absence of SS for 1D commensurate filling of $\rho = \frac{1}{2}$ [13, 47] and $\rho = 1$ [5, 49, 56]. In our thesis, we discuss in detail how this dimensionality [58] plays a role to get SS.

Chapter 4

Extended Bose-Hubbard Ladder

In the previous chapters, we discovered that in 1D EBHM, there are a reentrance behavior [35], BKT-type SF-MI transition [59], and no SS exists for $\rho = 1$. However, these are not the case in 2D or higher dimensions. These features of dimensionality in EBHM make it enjoyable to study dimensional crossover from 1D to 2D. On the other hand, as we believe that these behaviors can be related to the strong quantum fluctuation in low-dimensional physics [7, 27], it is best to consider a 2-leg ladder rather than a multi-leg ladder. Here we can study the effect of inter-leg coupling along with the strong fluctuation.

With this motivation, we have systematically studied ground-state phase diagrams of the two-leg ladder extended Bose-Hubbard model. Our main focus is to understand the role of inter-chain tunneling in the obtained phases. This type of bosonic ladder has also been studied using the Bosonization method [6, 60] and DMRG [10] earlier with different motivations. They showed that inter-chain tunneling increases the region of superfluidity [10], and can destroy the direct MI-HI transition by establishing an SF phase in the intermediate region [6]. These results hint that there is a possibility of a supersolid in the strongly correlated regime. However, complete phase diagrams of this model with supersolid and the role of interchain tunneling in it were never studied. Other studies with modified Bose-Hubbard ladder have found dimer superfluid in case of attractive on-site interaction [61], pair-superfluid where attractive inter-chain interaction [62–64] was introduced, fractional insulator phases in strong inter-chain coupling limit [65], and rung-pair localization with hard-core bosons [66].

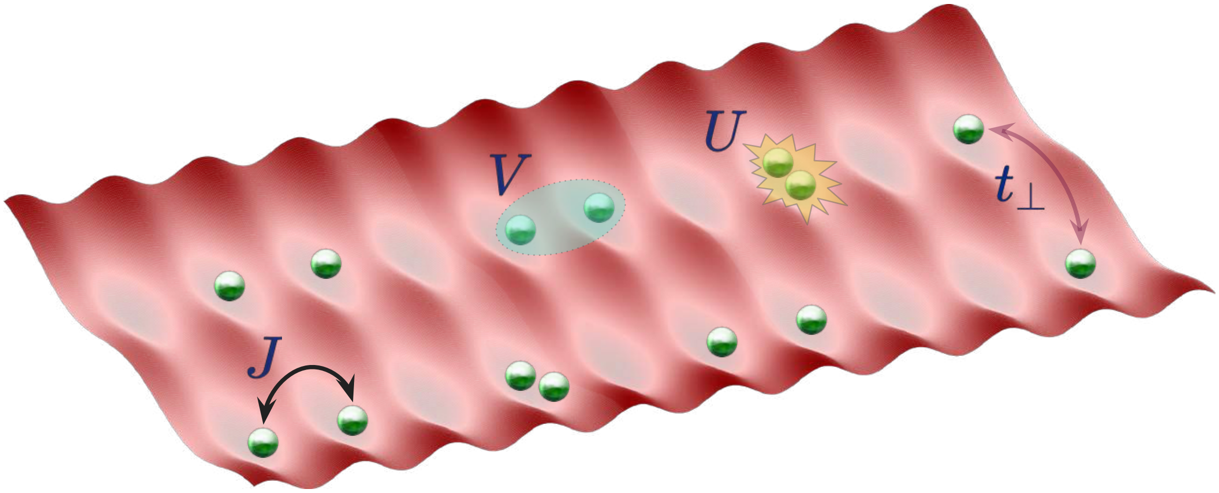

Figure 4.1: Schematic diagram for the ladder setup. J provides the inter-chain tunneling, V is the nearest-neighbor interaction along a chain, U is the strength of the on-site interatomic interaction, and $t_\perp$ is the inter-chain hopping.

4.1 Hamiltonian

We consider an extended Bose-Hubbard ladder, schematically shown in (fig. 4.1), described by the Hamiltonian [6, 10, 61, 65],

$$\begin{aligned} \hat{H} &= -J\sum_{i,\alpha}(\hat{b}^\dagger_{i,\alpha}\hat{b}_{i+1,\alpha} + \text{H.c.}) - t_\perp\sum_{i}(\hat{b}^\dagger_{i,1}\hat{b}_{i,2} + \text{H.c.}) \\ &\quad + \frac{U}{2}\sum_{i,\alpha}\hat{n}_{i,\alpha}(\hat{n}_{i,\alpha}-1) + V\sum_{i,\alpha}\hat{n}_{i,\alpha}\hat{n}_{i+1,\alpha}, \end{aligned} \tag{4.1}$$

where $\hat{b}^\dagger_{i,\alpha}(\hat{b}_{i,\alpha})$ is the bosonic creation (annihilation) operator and $\hat{n}_{i,\alpha} = \hat{b}^\dagger_{i,\alpha}\hat{b}_{i,\alpha}$ is the number operator at the site i in the leg-α as shown in fig.4.2. For two-leg ladder, $\alpha = 1,2$. Here we consider a symmetric ladder, where the parameters are equal in both legs. The parameters J and $t_\perp$, respectively, provide us intra-chain nearest-neighbor and inter-chain hopping strengths. U and V denote on-site inter-particle and the nearest-neighbor repulsive interaction in each chain, respectively. As we consider fixed ρ, (canonical case) we omit μ from the Hamiltonian. At $t_\perp = 0$, the Hamiltonian in Eq. (4.1) breaks up into two independent chains for EBHM, and the critical points match with the 1D model [15].

4.2 Method

We have used the matrix-product state (MPS) based density-matrix renormalization (DMRG) [11, 29, 67] algorithm implemented in TenPy package [68] for diagonalizing the Hamiltonian to get the many-body ground-state. The ground-state phase diagrams are obtained in open-boundary condition using finite-size scaling of order parameters and energy gap discussed in section.(3.2). We have performed simulations in $80 \leq L \times 2 \leq 160$ lattice sites with a maximal number of $n_{max} = 6$ bosons per site depending on the parameter values. For DMRG, we have used bond dimensions up to $\chi = 800$ and a maximum of 30 sweeps as needed for convergence (Appendix.A). The truncation errors in our calculation are always less than 10^{-6}. For the representative purpose, sometimes we have gone up to $L \times 2 = 400$ sites.

We have used $2N = 2L$, i.e., $\rho = 1$ for primary phase diagrams, where we may have missed HI, as explained in section(3.2.4). To recover HI, we also obtain some diagrams with $2N = 2(L+1)$. Later in the thesis, to show the effect of the rung, we also remove one central rung and obtain an un-scaled phase diagram for comparative purposes. To simulate the ladder Hamiltonian, we have mapped it to a 1D array of sites in a zig-zag fashion, as shown in fig.4.2.

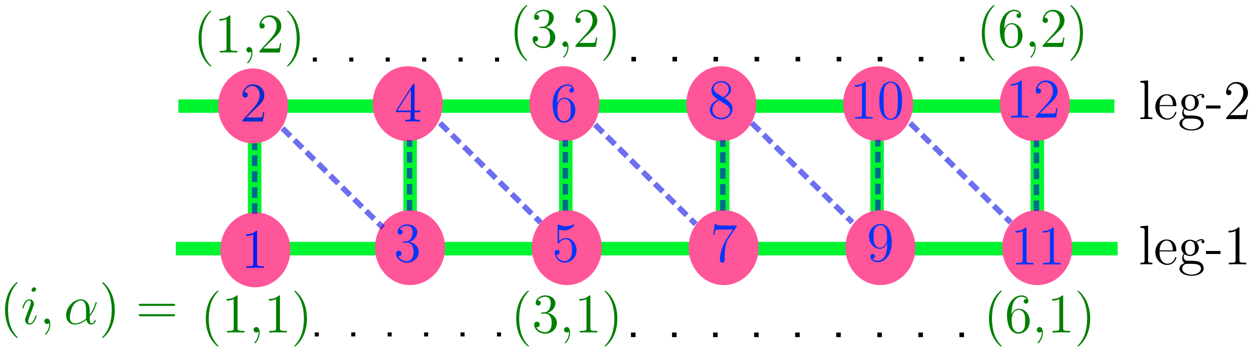

Figure 4.2: Mapping ladder sites to 1D-chain in a zig-zag way: sites at leg-1(leg-2) are mapped to odd (even) positions of the 1D chain. Here (i,α) denotes site i at leg-α.

4.3 Observables

For phase diagram: For characterising phases and identifying the phase-transition points, we mainly use following energy gap and correlation functions, similar to 1D EBHM (Table.3.1)-

$$\text{Charged gap:} \quad \Delta_L^c = E_L^0(N+1) + E_L^0(N-1) - 2E_L^0(N), \tag{4.2}$$

$$\text{DW order:} \quad \mathscr{O}^{\alpha}_{\text{DW}}(j,r) = (-1)^r \langle \delta\hat{n}_{j,\alpha}\delta\hat{n}_{j+r,\alpha}\rangle, \tag{4.3}$$

$$\text{String order:} \quad \mathscr{O}^{\alpha}_{\text{string}}(j,r) = \left\langle \delta\hat{n}_{j,\alpha} \exp\left\{ i\pi \sum_{j\le k<j+r} \delta\hat{n}_{k,\alpha} \right\} \delta\hat{n}_{j+r,\alpha} \right\rangle, \tag{4.4}$$

where (j,α) denotes the site j at leg-α. All the correlation functions are measured in the intra-leg direction and it is symmetric in both legs. Then these are scaled with different single-leg lengths L as similar to the 1D case (section.3.2.1). L in the charged gap Δ^c_L denotes the single-leg length L and we calculate on the whole system of $2L$ lattice sites with $\{2N, 2N\pm 1\}$ particles. We use this 'L' [10] while calculating $L\Delta^c_L$ for the scaling (section.3.2.2). If someone considers $2L\Delta^c_L$ for the purpose, it doesn't affect the phase diagram much from what we have used. As numerical tolerance, here also we use $\Delta^c_L \Delta L = 0.04$ as numerical zero.

Correlation functions for better understanding: To understand the phases and their characteristics better, we calculated following correlation functions (also shown in fig.4.3) -

$$\text{SF correlation fn:} \quad \Gamma^{\alpha}(j;r) = \langle \hat{b}^{\dagger}_{j,\alpha}\hat{b}_{j+r,\alpha}\rangle, \tag{4.5}$$

$$\text{Rung correlation:} \quad \gamma(j) = \langle \hat{b}^{\dagger}_{j,1}\hat{b}_{j,2}\rangle, \tag{4.6}$$

$$\text{Rung-rung corr.:} \quad \gamma^{\parallel}(j;r) = \langle \hat{b}^{\dagger}_{j,2}\hat{b}_{j+r,2}\hat{b}^{\dagger}_{j+r,1}\hat{b}_{j,1}\rangle - \langle \hat{b}^{\dagger}_{j,2}\hat{b}_{j,1}\rangle\langle \hat{b}^{\dagger}_{j+r,1}\hat{b}_{j+r,2}\rangle \tag{4.7}$$

$$\text{Rung-leg corr.:} \quad Rl(j;r) = \langle \hat{b}^{\dagger}_{j+r,1}\hat{b}_{j+r,2}\hat{b}^{\dagger}_{j+r,2}\hat{b}_{j,2}\rangle - \langle \hat{b}^{\dagger}_{j+r,1}\hat{b}_{j+r,2}\rangle\langle \hat{b}^{\dagger}_{j+r,2}\hat{b}_{j,2}\rangle \tag{4.8}$$

where j defines an initial position and r denotes the distance from it. To remove the dependence of j, all the above correlation functions are averaged over j for fixed r inside the bulk region. We consider this j-independent correlation function as a result, which is a function of only r. Notice, we do not add Hermitian conjugate (h.c.) to the correlation functions because the Hamiltonian is time-reversal symmetric, and the wave function is real. We have also checked this within the numerics.

SF-correlation [Γ^{α}(r)] is measured along the leg-direction, and it is symmetric in both legs for all the phases. Rung-correlation [$\gamma(j)$] defines the hopping of particles along the rung direction, which says how strongly particles are exchanged between legs, and in turn, describes the role of $t_{\perp}$. With the onset of DW-order, the lattice is divided into even-odd sites, so we average over *even* and *odd* sites separately.

Rung-rung correlation [$\gamma^{\parallel}(r)$] is a 4-point correlation function, characterizing correlated hopping in two-rungs at a distance of r. In simple words, it measures if in one rung, particle tunnels from lower chain to upper-chain, then how much probable it is that another particle will also tunnel from upper-chain to lower-chain at a distance r. A close look at this captures the effect of intra-chain repulsive interaction V. Remember, the direction of these two hopping should be opposite (fig.4.3).

Similar to the rung-rung correlation, the rung-leg correlation $[Rl(r)]$ measures if one particle tunnels on a rung from one leg, does another particle in that leg come to fill up the position. This would help us understand how the hopping at rung can amplify the particle delocalization along the leg. Here, we selectively chose one leg because both legs are symmetric. All these four-point correlation functions are connected correlation functions, which we use to subtract the effect of independent tunneling.

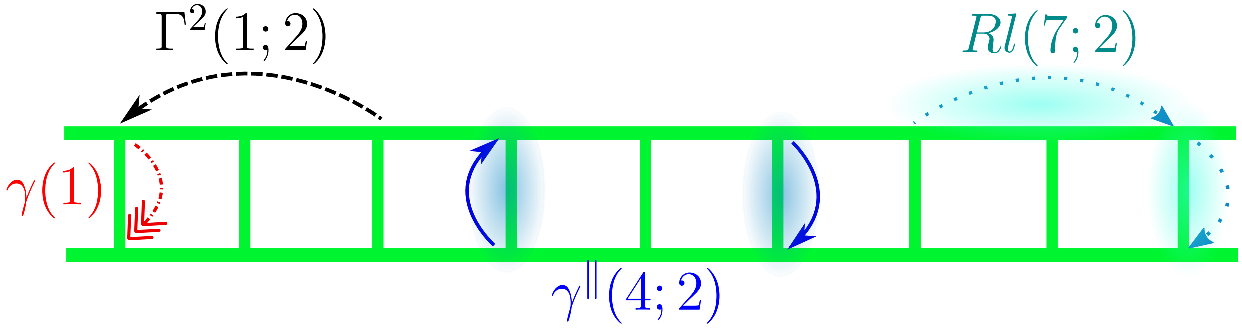

Figure 4.3: Schematic of different correlation functions: $\gamma(1)$ defines hopping-correlation on rung at site-1; $\Gamma^2(1;2)$ defines SF-correlation function at site-1 of leg-2 for distance r=2 ; $\gamma^{\parallel}(4;2)$ measures connected rung-rung correlation between site-4 and site-(4+2) ; the rung-leg correlation $Rl(7;2)$ tells us if one particle hops at rung (7+2) from leg-2 to leg-1, does another particle hop from site-7 to site-(7+2) of the leg-2?

Compressibility: Compressibility is an alternative way to understand if a phase is gapped or gapless. It measures if some energy is put into the system or taken out, does the system accommodates one extra or less particle. We first define the chemical potential μ of the system with density $\rho = N/L$ as

$$\mu = \frac{\delta E_L^0(N)}{\delta N} \tag{4.9}$$

and from the behavior of ρ as a function of μ, we can identify a gapped and gapless phase [53]. The compressibility κ, which is non-zero in the gapless phase, is calculated as

$$\kappa = \frac{\delta \rho}{\delta \mu} \tag{4.10}$$

For a gapped phase, by changing $\delta\mu$ amount of energy, the system cannot accommodate $\delta\rho$ particles, and that's why $\kappa = 0$ in it. We will use κ later to show that for $\rho = 1$, although in 1D there is no SS ($\kappa = 0$), there is a non-zero region SS in the ladder.

Excitation spectrum: We know that with onset of DW-order, there is a roton instability in the excitation spectrum $\Omega(k)$ [12]. A good approximation for $\Omega(k)$ along the leg-direction can be found by using the expression [56],

$$\Omega(k) = \frac{E_k}{LS(k)} \tag{4.11}$$

Here $E_k = \frac{-J}{L}[\cos k - 1]\langle\Psi_0|\sum_{i=1}^{L}(b_i^{\dagger}b_{i+1} + h.c)|\Psi_0\rangle$ and $|\Psi_0\rangle$ is the ground state. The structure factor is defined as, $S(k) = \frac{1}{L^2}\sum_{x,x'} e^{ik(x-x')}\langle n(x)n(x')\rangle$. Here, k is the usual wave-vector. We later show the roton-instability of $\Omega(k)$ in the SS region.

Entanglement: We calculate von-Neumann entanglement for different bipartitions and entanglement spectrum in different phases. For that purpose, the ladder is divided into two halves (along the leg or rung) and write $|\Psi\rangle$ in Schmidt decomposition-

$$|\Psi\rangle = \sum_{\beta=1}^{\chi} \Lambda_\beta |\beta\rangle_L |\beta\rangle_R \tag{4.12}$$

where Λ_β is Schmidt coefficient and $|\beta\rangle_L$ and $|\beta\rangle_R$ are the orthonormal Schmidt basis, for the left and right half [35], with normalization $\sum_\beta \Lambda_\beta^2 = 1$. Due to MPS ansatz (Appendix. A), the maximum allowed Schmidt rank is the maximum bond-dimension χ. Using Schmidt coefficient Λ_β, we can define the entanglement entropy as -

$$S_l = -\sum_{\beta=1}^{\chi} \Lambda_\beta^2 \log_2(\Lambda_\beta^2) \tag{4.13}$$

where l defines the length of the segment or in our case considers the length of the left-half. Now, we will define the different configurations for which we calculate this entanglement entropy.

(a) Between two legs [fig.4.4(a)], which is done by taking partial trace over one-leg

(b) Dividing the ladder in chain-direction [fig.4.4(b)], which is done by using left-right segment of middle bond while doing DMRG sweep.

We also calculated the entanglement spectrum (ξ_β) for the bond in the middle of both chains

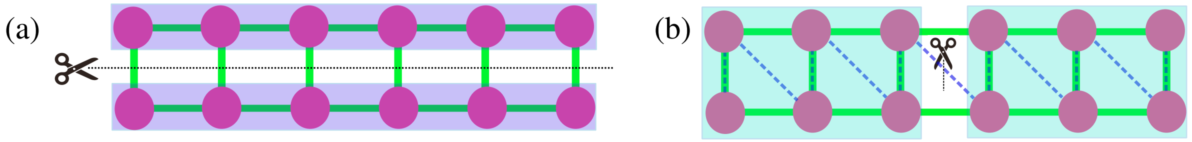

Figure 4.4: Different bipartitions to calculate entanglement : **(a)** For entanglement between two legs; **(b)** For entanglement along the leg direction, by cutting at the middle-bond as shown

(fig.4.4(b)). It is defined as energy states of a fictitious Hamiltonian $\mathscr{H}$ by equating it to with the density matrix as $\rho_l = e^{-\mathscr{H}}$ [69], which implies

$$e^{-\xi_\beta} = \Lambda_\beta^2 \tag{4.14}$$

We can learn about the superposition states of a phase by looking at the degeneracy spectra of ξ_β, as Λ_β defines different superposition states.

4.4 Experimental Setups

We suggest two possible experimental setups that can model our Hamiltonian (eq.4.1). For obtaining on-site interaction (U/J) and inter-chain tunneling ($t_\perp$), we can use ultra-cold atomic [70] optical-lattices (Appendix. B). For independent control in the leg and rung direction, we can use different depths of optical lattices. Getting the repulsive nearest-neighbor interaction (V) along the leg direction but not in the rung direction is tricky. For that, we suggest using dipole-dipole interaction or Rydberg-dressed atoms.

Dipolar interaction: In dipolar gases or polar atoms/molecules [36, 37], after polarization, all dipoles point in the same direction, and the dipole-dipole interaction energy between such two polarized dipoles is given by [16]-

$$V_{dd}(r,\theta) = \frac{C_{dd}}{4\pi}\frac{(1-3\cos^2\theta)}{r^3} \tag{4.15}$$

where θ is the angle between the common polarization axis and the relative position ($\vec{r}$). The coupling constant $C_{dd} = \mu_0\mu_m^2$ for particles having magnetic dipole moment μ_m (where μ_0 is the vacuum permeability) and $C_{dd} = \mu_e^2/\varepsilon_0$ for particles having a permanent electric dipole moment μ_e (where ε_0 is the vacuum permittivity) . To selectively get dipole interaction only in the leg direction, we will use the anisotropy of this interaction. When two dipoles sit side-by-side ($\theta = 90^\circ$) along the leg-direction, they have repulsive interaction ($V_{dd} > 0$). On the other hand, we can choose θ between two dipoles on a rung as $\cos^{-1}(1/\sqrt{3})$, such that $V_{dd} = 0$. The setup is shown in fig.4.5, where all dipoles lie in the x-y plane and are polarized along the y-z plane, making an angle of $\theta = \cos^{-1}(1/\sqrt{3})$ with the x-y plane ($\vec{r}$ also lies in the x-y plane as shown).

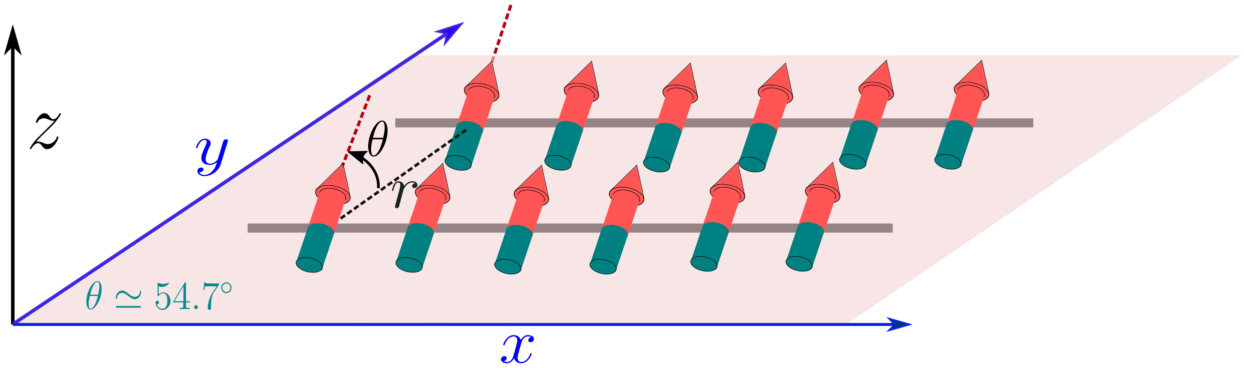

Figure 4.5: Experimental setup-1 for extended Bose-Hubbard ladder using dipolar interaction: all dipoles are polarized along the y-z plane, and lie in the x-y plane making an angle of $\theta = \cos^{-1}(1/\sqrt{3})$ with the plane

Rydberg-dressed atoms: In this setup, we use anisotropy of Rydberg interaction to model the ladder Hamiltonian. We can weakly admix Rydberg states $|r\rangle$ with the ground state of Bosons $|g\rangle$ using Rabi frequency Ω, along with large negative detuning ($|\Delta| \gg \Omega$) [24] as shown in fig.4.6. Here we consider laser-excited Rydberg $^2P_{3/2}$ state of Rubidium atoms, denoted by $|r\rangle = |n^2P_{3/2}, m = 3/2\rangle_z = |np, 1\rangle_z |\frac{1}{2}\frac{1}{2}\rangle_z$. Van der Waals interaction V_{rr} between these Rydberg-dressed states has an approximate form of [17]

$$V_{rr}(r,\theta) = \left(\frac{\Omega}{2|\Delta|}\right)^4 \frac{C_6(\theta)}{r^6 + R_c^6} \quad ; \quad C_6(\theta) = (ea_0)^4 n^{11} \sin^4\theta \tag{4.16}$$

where the strength can be tuned by principal quantum number n, and as it decays as $\frac{1}{r^6}$, we can approximate it to nearest-neighbor interaction. e is the charge of an electron, a_0 is the scattering length, and θ being the angle between the quantization (here z) axis and the relative vector r. R_c defines the blockade radius $R_c = [C_6/2\hbar|\Delta|]^{1/6}$. Using this anisotropy, we can have zero interaction with $\theta = 0$ (put in the rung direction), and the strongest at $\theta = \pi/2$ (along the leg direction). We have the ladder in the z-x plane and rung along the z-direction (fig.4.6).

To understand this anisotropy, consider the initial state in $|r\rangle$, which has the $|np,1\rangle_z$ part. By emitting a photon, this state can go to $|ns,0\rangle_z$ (see **A** in fig.4.6), whereas the photon can go in either z-direction with σ_+ polarization or to x-direction with linearly polarized light along the y-direction. As the other $|r\rangle$ is already in $|+1\rangle$ state (**B**), σ_+ polarised light cannot be absorbed, which means along z-direction(rung) there is no interaction i.e $V_{rr}(\theta = 0) = 0$. On the other hand, as π_y involves both σ_+ and σ_-, a transition is possible (**C**), and the photon can be absorbed. That's how there can be interaction along the x-direction (leg), i.e. $V_{rr}(\theta = \pi/2) \neq 0$.

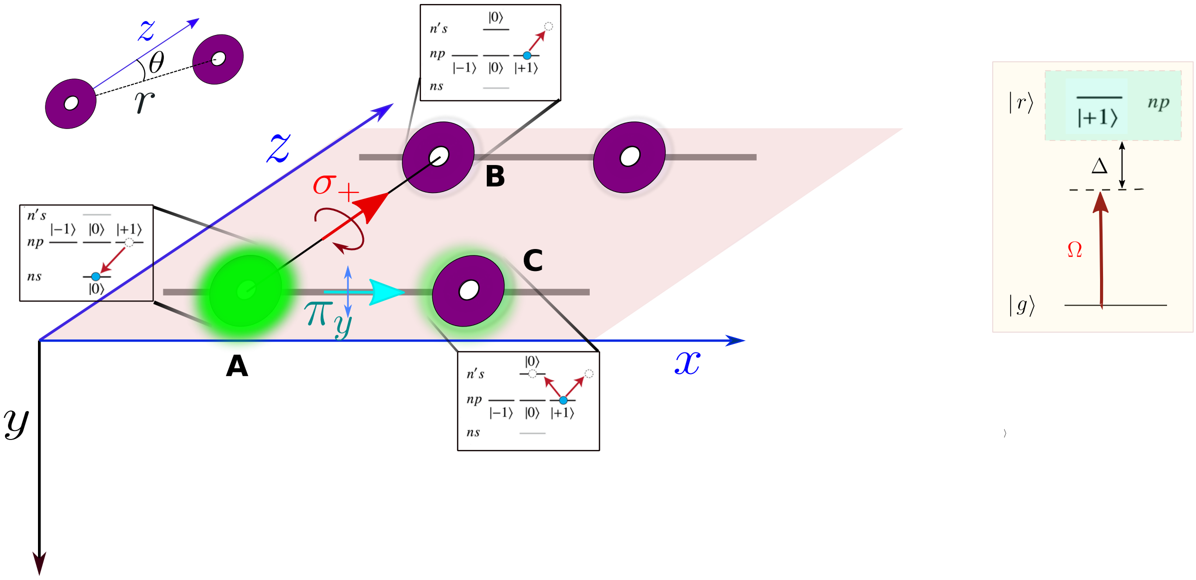

Figure 4.6: **Left:** Experimental setup-2 for extended Bose-Hubbard ladder using Rydberg-dressed atoms: all the atoms lie in the x-z plane, where the p-orbital lobes are in x-y plane. Along the z-direction, due to σ_+ polarization of a photon, A cannot interact with $|r\rangle$ at B, whereas due to π_y polarization along x-direction A can interact with C. **Right:** Ground state ($|g\rangle$) being weakly coupled to a Rydberg state ($|r\rangle$) by a laser field of Rabi frequency Ω and detuning Δ

Chapter 5

Results and Discussions

In this chapter, we discuss the results for the symmetric extended Bose-Hubbard ladder introduced in chapter-4 using the methods and observables mentioned therein. We work with the constant filling factor $\rho = 1$ and set the energy scale by choosing $J = 1$.

5.1 Weak on-site interaction

For weak on-site interaction, here $U/J = 2$ (fig.5.1), we have obtained a phase diagram in $(t_\perp, V)$ plane, where we observe supersolid (SS) sandwiched between superfluid (SF) at small V and density waves (DW) at large V, for $t_\perp \neq 0$. However, no Mott insulator (MI) is there because U/J is below the critical point of SF-MI transition in 1D, which is $(U/J)_c = 3.61$ [31]. As there is no SS in this parameter regime of the 1D EBHM model, i.e., when inter-chain tunneling $t_\perp = 0$ (sec.3.2.2), it must be the non-zero $t_\perp$ in the ladder, which plays the leading role in having SS. We can explain why SS is less probable in 1D than in a ladder in this manner - in the 1D lattice, V wants to localize particle-hole pairs on the same lattice sites, where J tries to delocalize. In other words, for 1D, there is no other channel for particles to delocalize without strictly opposing the strong repulsion of V. However, the inter-chain tunneling serves as an extra-channel to simultaneously allow superfluidity and density waves in the ladder. A possible mechanism can be due to inter-chain tunneling; particle-hole pairs are created on the rungs, enhancing the delocalization of particles along the leg direction.

In fig.5.1, we can see that the SF-SS transition line has a weaker dependence on $t_\perp$. This can be explained as this line is defined by the onset of $\mathcal{O}_{DW}$ along the leg-direction, and $t_\perp$ cannot affect that directly. On the other hand, the critical points (V_c) for the SS-DW line increase with $t_\perp$ till $t_\perp \sim 0.8$, after which it saturates to that value of V_c. The first increase of the SS region in low $t_\perp$ is expected, as with increasing $t_\perp$, the particles are getting more delocalized, increasing the superfluidity in the regime DW-order is already present. As a signature, we show in fig.5.2(b), for V=4.5, how with increasing $t_\perp$ the $L\Delta_L^c$ coalesces at $t_\perp = 0.5$, signifying the gapped-DW to gapless-SS transition. We can also see the increase in the SF-correlation function, shown in the inset. The saturation behavior after certain $t_\perp$ is expected as $t_\perp$ can affect only one lattice distance along the rung in a *two*-leg ladder, and it cannot increase the superfluidity indefinitely through only one rung distance. With more legs, we expect this saturation of $t_\perp$ to shift towards a higher value. Similar saturating behavior is also observed in the critical points (U_c) for SF-MI transition in a bosonic ladder [10]. One of the major obstacles in the past about observing SS was its existence in tiny phase space [71]. However, here we found quite a large region of SS, which may help in detecting SS. To support the existence of SS in this large region, we show coalescing $L\Delta_L^c$ for different L at DW-SS transition and scaled V_c for SF-SS transition in fig.5.2(a) at $t_\perp = 0.6$.

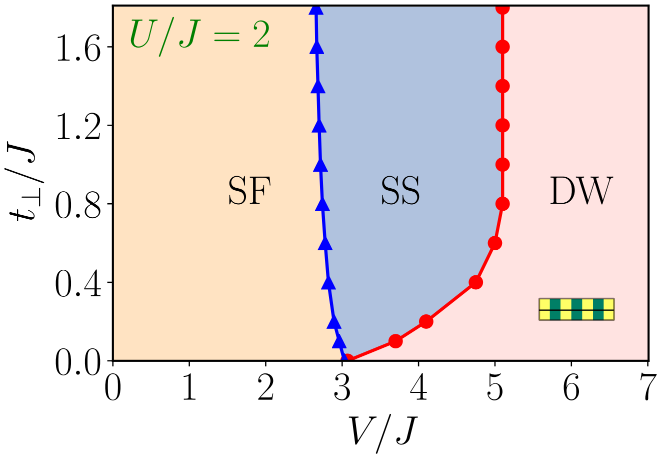

Figure 5.1: Phase diagram in $(t_\perp, V)$ plane for U=2: SF, SS, and DW are observed. SF-SS remains almost constant with increasing $t_\perp$, whereas the SS-DW line first increases towards the right and then saturates (SF: superfluid, SS: supersolid, DW: density wave). **Inset:** pattern of density wave is symmetric on both legs.

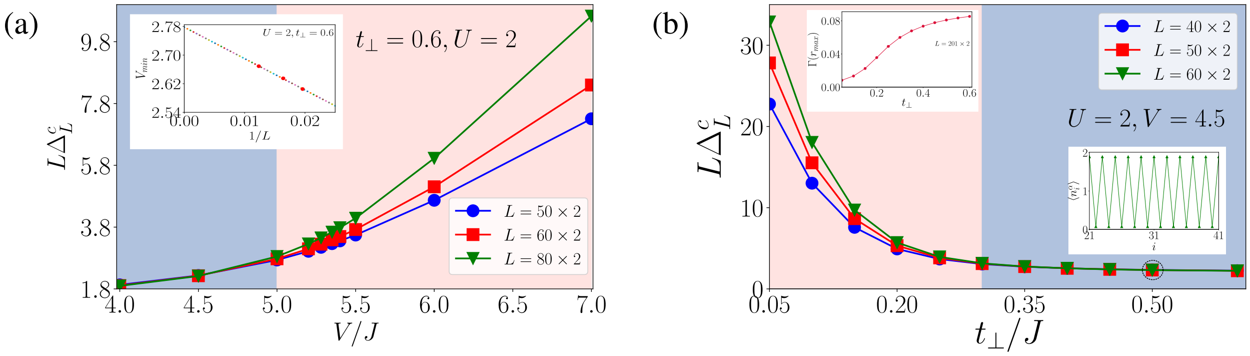

Figure 5.2: Coalescing $L\Delta_L^c$ for DW-SS transition: **(a)** With decreasing V $L\Delta_L^c$ for different L coalesces at DW-SS transition point $V_c = 5$ for $t_\perp = 0.6, U = 2$, **Inset:** From linear fit of V_{min} for $\mathscr{O}_{DW}$ with $1/L$, SF-SS transition obtained at V_c=2.78 **(b)** With increasing $t_\perp$, $L\Delta_L^c$ for different L coalesces at DW-SS transition point $t_\perp^c = 0.3$ **Inset(top left):** With increasing $t_\perp$, $\Gamma(r_{max})$ also increases, **Inset(bottom right):** Existence of density pattern in SS phase ($t_\perp = 0.5$).

5.2 Strong on-site interaction

With strong on-site interaction, specifically $U/J = 6$ case here, main features of the phase diagram discussed in U=2 case (fig.5.1) is also present here (fig.5.3), however with a smaller region of SS. The SS region is suppressed due to large U in which case occupying any sites with more than one particle is costlier, whereas superfluidity needs particle-hole excitation. U/J being greater than MI-SF transition, MI is observed in the low $t_\perp$ region which then vanishes to SF with increasing $t_\perp$. For $V = 0$, the MI-SF critical point matches with Luthra *et al.* [10]. We show how $L\Delta_L^c$ coalesces at MI-SF transition in fig.5.3(b). Unlike the $U = 2$ case, effect $t_\perp$ saturates at large $t_\perp \sim 1.8$, which means it is not easy for $t_\perp$ to overcome the effect of strong U in order to get saturated.

5.3 Effect of $t_\perp$ on n_{max}

For drawing the phase diagrams we mostly use $n_{max} = 5$ and $n_{max} = 6$ bosons per site, as per the requirement for energy convergence with respect to n_{max}. Here, we observe that the need for a larger n_{max} is prominent in the large $t_\perp$ regime as shown in fig.5.4(a). For $n_{max} = 2$, huge energy difference is expected, as this is only good for an insulator phase, where particles are not tunneling to an occupied site. However, in the SF region, using $n_{max} = 2$, is not at all good. With this knowledge at first, we expected that $n_{max} = 4$ should be good enough, and drew a phase diagram using it as shown in fig.5.4(b). There we found a reentrance of DW-SS-DW with increasing $t_\perp$.

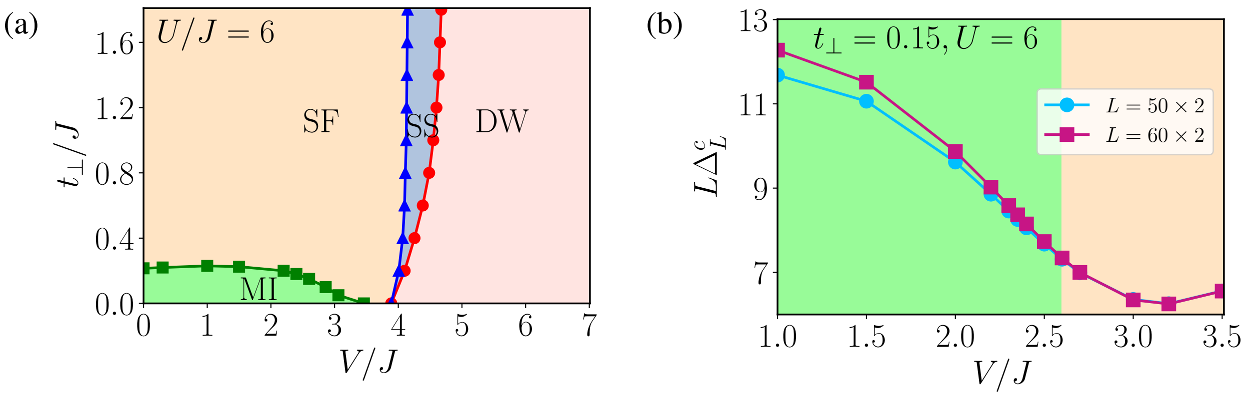

Figure 5.3: **(a)** Phase diagram in $(t_\perp, V)$ plane for U=6: MI is observed for small V and small $t_\perp$, along with SF, SS and DW **(b)** For $t_\perp = 0.15$, with increasing V, $L\Delta_L^c$ for different L coalesces at MI-SF transition point V_c=2.6

One possible reason behind this can be related to the effect of $t_\perp$ as discussed in section 5.1. Due to the lack of allowed bosons at sites, the superfluidity cannot be increased as possible by $t_\perp$, and in the strong $t_\perp$, it reduces the region of SS. If in an experimental setup, the maximum number of bosons at a site can be fixed, this reentrance can be observed, by choosing lesser n_{max}. Thus n_{max} can be an extra knob to control the phases.

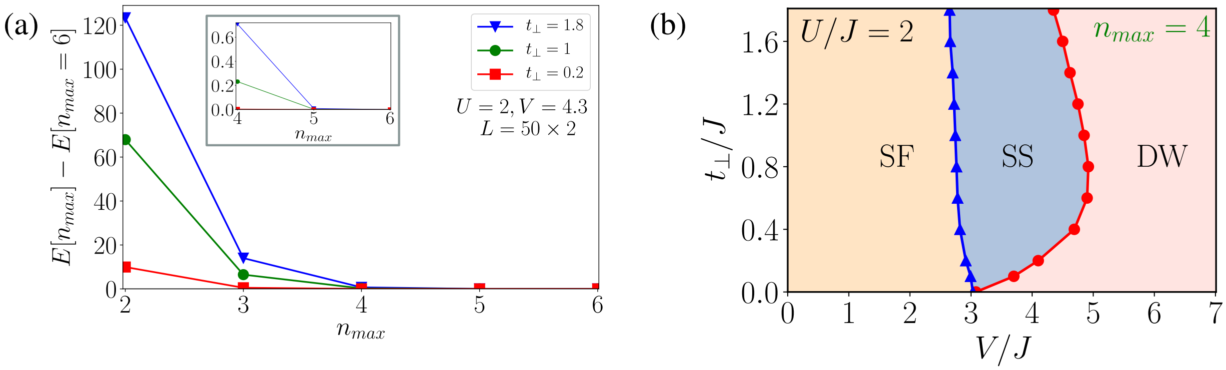

Figure 5.4: Effect of n_{max} : **(a)** With increasing n_{max} energy converges. For larger $t_\perp$, more n_{max} is necessary (**Inset:** Enlarged version of the same plot to show for $n_{max} = 4$.) **(b)** Phase diagram with $n_{max} = 4$, where convergence reaches with $n_{max} \geq 5$: a reentrance of DW-SS-DW is observed at fixed V

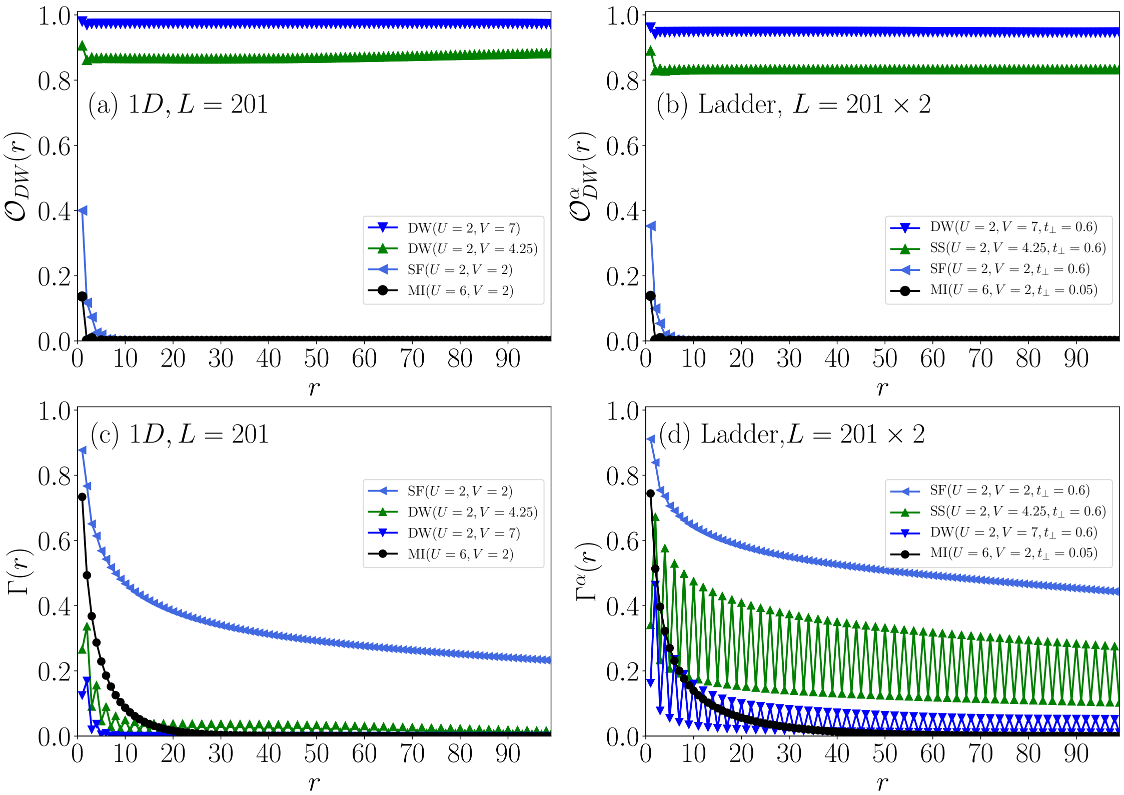

Figure 5.5: DW-order and SF-correlation function for different phases in 1D and ladder: **(a), (c)** $\mathcal{O}_{DW}$ and $\Gamma(r)$ respectively for different phases in 1D EBHM, where SS does not exist; **(b), (d)** $\mathcal{O}^{\alpha}_{DW}$ and $\Gamma^{\alpha}(r)$ respectively for different phases in the ladder, where SS exists

5.4 Evidences of SS in ladder

DW-order and SF-correlation: To support the existence of SS in the ladder which is not present in 1D EBHM, we have shown how $\mathcal{O}^{\alpha}_{DW}(r)$ and $\Gamma^{\alpha}(r)$ decays with r, for all the 4 different phases in fig.5.5 both in 1D and ladder. As expected, the MI and SF have zero DW-order, whereas the DW and SS have non-zero order. On the other hand, in DW and MI phase, the SF-correlation function [(c),(d)] decays to zero, whereas in SF and SS, although it decays, it does not go to zero. For U=2, V=4.25, in 1D ($t_\perp = 0$), we can see $\Gamma(r)$ decays to zero proving it to be in DW phase, whereas in the ladder with $t_\perp = 0.6$, $\Gamma(r)$ has non-zero values showing the existence of SS with the same (U,V) value. To mention, the effect of Z_2 symmetry breaking can be seen in Γ^{α} of DW and SS.

Compressibility: In fig.5.6 (a), we can see a plateau of constant $\rho = 1$, despite the change in μ, which results in zero compressibility (section.4.3), and we don't have SS for $\rho = 1$ in 1D.

With the same (U,V) value, when $t_{\perp} = 0.6$, we observe non-zero compressibility in $\rho = 1$ region, which supports the existence of SS in ladder. Similarly, in DW of Ladder, zero compressibility is observed in $\rho = 1$ as expected.

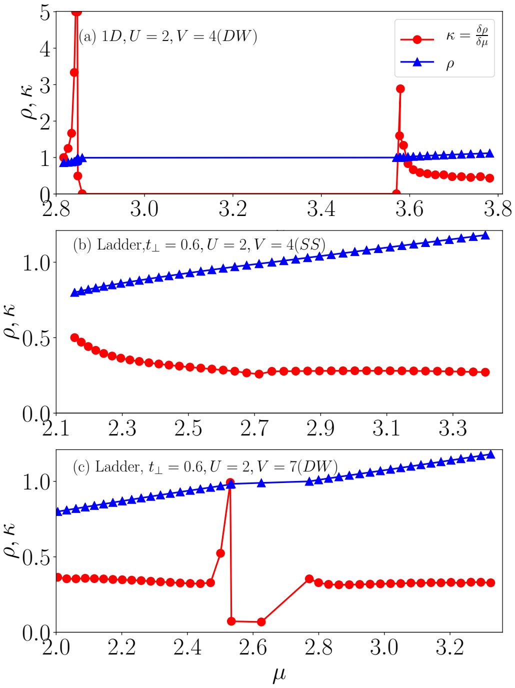

Figure 5.6: Variation of compressibility(κ) and density(ρ) with chemical potential(μ) : **(a)** For 1D, the plateau of $\rho = 1$ have zero compressibility signifying DW, while it is finite elsewhere showing the existence of SS, **(b)** Non-zero value of compressibility throughout $\rho = 1$ in this parameter regime of ladder proves existence of SS, which is not present in (a), **(c)** For DW in the ladder, the plateau of zero compressibility appears at $\rho = 1$

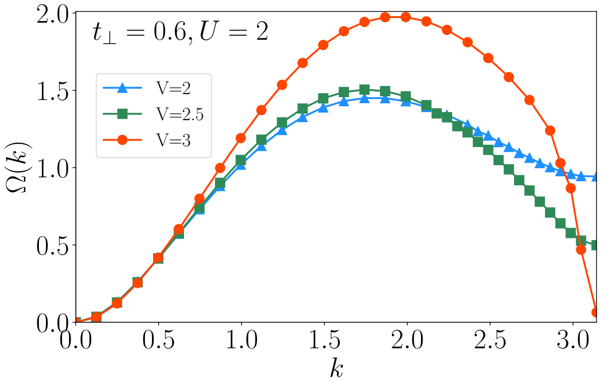

Figure 5.7: The dispersion relation, $\Omega(k)$ vs k for different V: Roton instability at SF-SS transition

Excitation spectrum: In fig.5.7, we can see for $V = 2$, in the SF phase, the roton minima of the excitation spectrum (along leg) is stable, and with increasing V it softens. At $V = 3$, the minima pinch the k-axis, which indicates the roton-instability. Thus it proves the existence of SF-SS transition.

5.5 Effect of $t_\perp$ and V on correlation functions

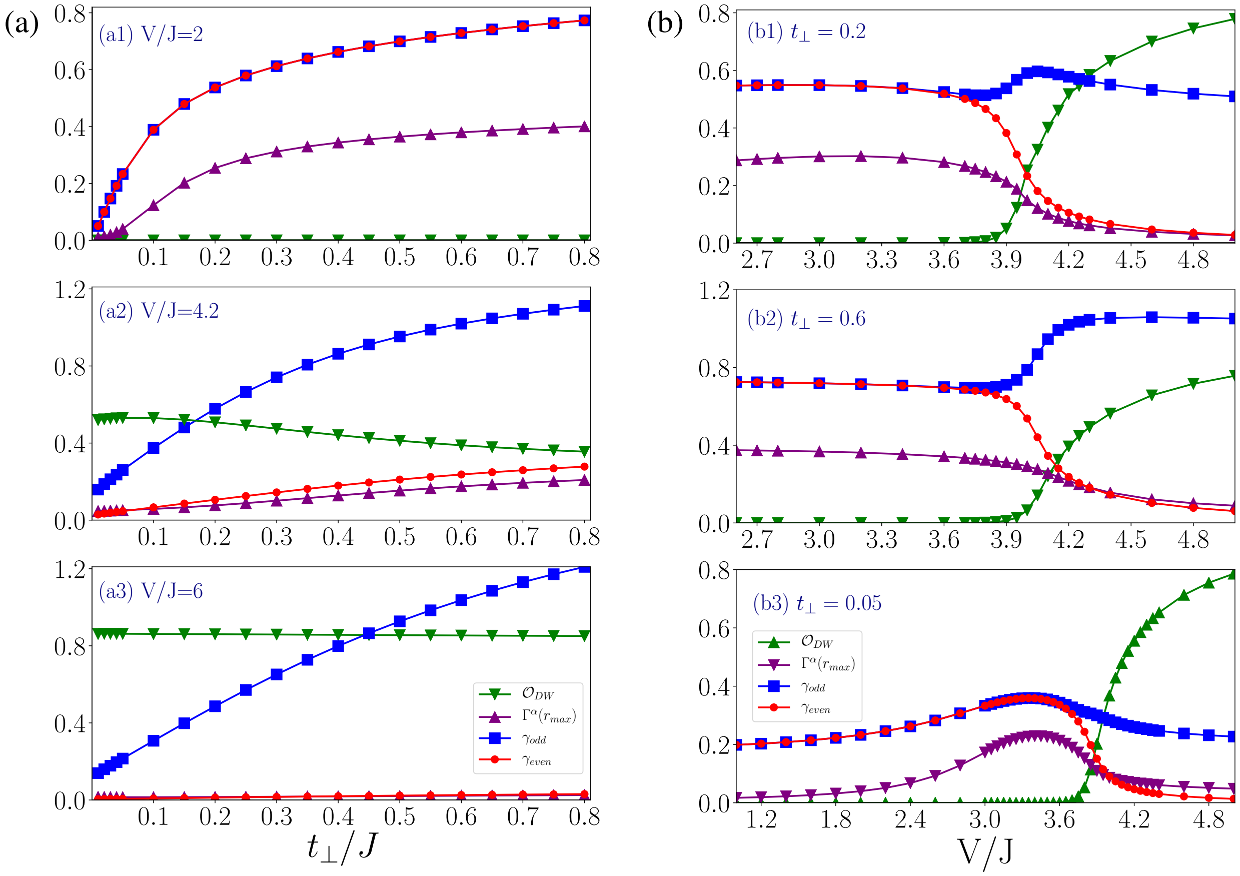

Figure 5.8: Effect of $t_\perp$ and V on correlation functions for U=6 in a $L \times 2 = 51 \times 2$ lattice : **(a)** Effect of increasing $t_\perp$ on (a1) MI to SF (a2) DW to SS (a3) DW **(b)** Effect of increasing V for (b1) $t_\perp = 0.2$ (b2) $t_\perp = 0.6$ (b3) $t_\perp = 0.05$

Effect of increasing $t_\perp$: Now, we will discuss how does correlation functions change with increasing $t_\perp$ in different phases [fig.5.8(a)], namely in MI, SF, SS and DW. In MI and SF (V=2), $\mathcal{O}_{DW}$ constantly remains at zero even with increasing $t_\perp$, indicating that strong repulsion (V) is the key player to have $\mathcal{O}_{DW}$. However, when the phase already has $\mathcal{O}_{DW}$, e.g.- in SS (a2) or DW (a3), increasing $t_\perp$ reduces it. This is probably the reason why we found slight bending of the $SF - SS$ line towards the right in fig.5.3(a). $\Gamma^\alpha(r_{max})$ is defined as the SF-correlation function at maximum possible distance r_{max} inside the bulk of a fixed lattice size. This is also the minimum of $\Gamma(r)$ out of all possible r. We can see that $\Gamma(r_{max})$ increases for MI-SF transition and after that in the SF region (a1). Although the same is true for SS (a2); in the DW-region (a3), it doesn't increase with $t_\perp$, which makes the phase insulating. The rung correlation function γ doesn't break Z_2 symmetry in SF region (a1), due to zero $\mathcal{O}_{DW}$, whereas in SS(a2) and DW(a3) region, it divides into γ_{odd} and γ_{even}. As we consider $L = odd$, the odd sites are occupied with 2's, whereas the even sites are 0's. This makes the γ_{odd} grow larger with $t_\perp$, where the effect in γ_{even} is very small (a3), due to 0's at even sites. As $t_\perp$ enhances the superfluidity along the leg, when the even rungs fail to have a non-zero correlation, the effective superfluidity in the leg-direction (Γ^α) is also lost (a3).

Effect of increasing V: When V is increased for fixed $t_\perp$, we observe the expected transition from SF to SS for $t_\perp = 0.2$ (b1) and $= 0.6$ (b2), shown by the onset of $\mathcal{O}_{DW}$ as the green-line. The existence of SS is understood by looking at the purple line (Γ_{SF}) in (b1) and (b2). It is not suddenly going to zero, with the onset of DW-order [4]. In (b3), we can see an increase of superfluidity from MI, with increasing V. It is non-trivial, as V should induce an insulator state rather than SF. However, this is not special to the ladder, as we can see the existence of SF in $t_\perp = 0$ also [15], and may be due to the gapless edge mode in that region [41].

5.6 Phase diagram in (U,V) plane for fixed $t_\perp$

We found out in fig.5.1 and fig.5.3 that depending on U, the area of SS-region changes. To understand this U-dependence, we fix $t_\perp = 0.6$, and draw the phase diagram in (U,V) plane (fig.5.9). We can see that the SF-SS line, which is defined by the onset of $\mathcal{O}_{DW}$, shifts towards large V_c with increasing U as expected, due to the competition between U and V. In the strong U limit, occupying multiple particles at a site costs more energy, and that is why non-zero $\mathcal{O}_{DW}$ is only possible in large V for large U (fig.5.10(d)). The most interesting part is the reentrance behavior observed in the SS-DW transition line. For fixed V, by increasing U, one goes from SS to DW to SS again.

It should be clear that $t_\perp$ has more effect on the SS-DW line than the SF-SS line, as $t_\perp$ affects the superfluidity, not DW-order. Now, for superfluidity, we consider the combined effect of $t_\perp$

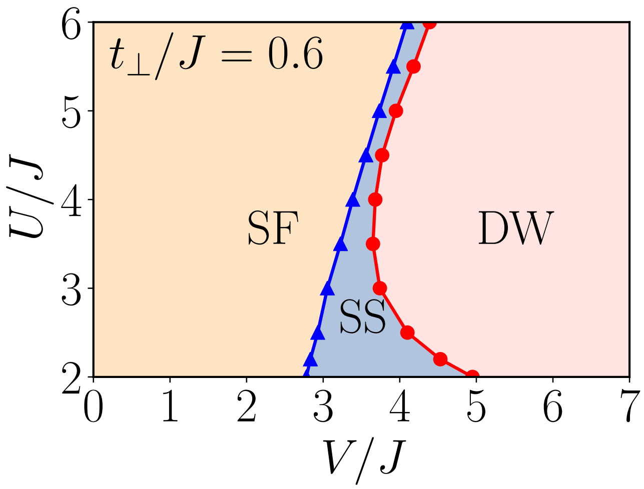

Figure 5.9: Phase diagram in (U,V) plane for $t_\perp = 0.6$: SF, SS and DW phases. A reentrance of SS-DW-SS is observed for fixed V. (SF: superfluid, SS: supersolid, DW: density wave)

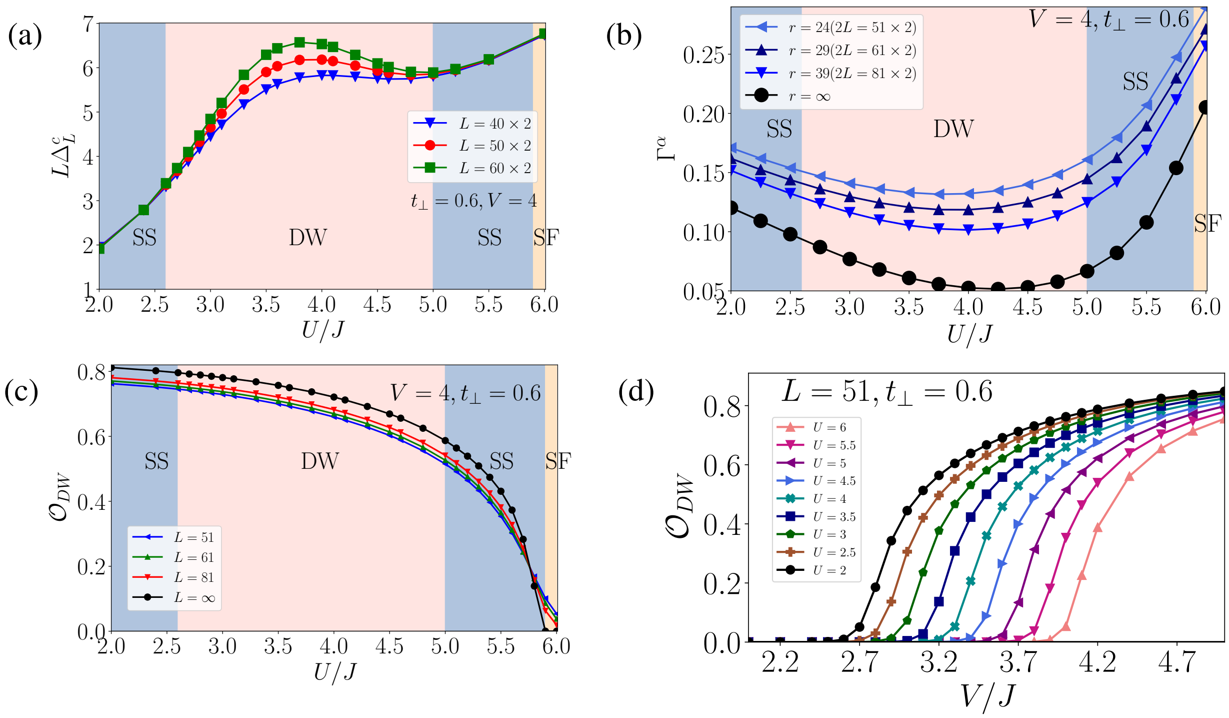

Figure 5.10: $L\Delta_L^c$, $\Gamma^\alpha(r)$ and $\mathcal{O}_{DW}$ showing the existence of reentrance: **(a)** $L\Delta_L^c$ shows the reentrance from gapless to gapped to gapless phase, **(b)** SF-correlation function showing a proof SS-DW-SS transition : lower at DW, but higher in SS at both sides for all L, **(c)** $\mathcal{O}_{DW}$ for different L throughout the reentrance shows existence of DW-order in SS and DW, **(d)** $\mathcal{O}_{DW}$ arises at larger V for larger U

and J, which surpasses the strength of U, when U is small. That is why in $t_\perp = 0.6$, although for $U \geq 4$, the SS-DW line can be seen as a competition between U and V, in case of small U, it is indeed competition between J and V (fixed $t_\perp$). When we plot in the $(U/J, V/J)$ plane, due to these different pairs of competition, we cannot directly compare the SS-DW line for small and large U, and a reentrance behavior occurs. Even in the phase diagram of 1D EBHM (fig.3.6), we can see how small U and large U behave linearly, and we believe ladder configuration shifts that behavior to an even larger U/J value with the help of $t_\perp$.

To support the existence of this reentrance, we have plotted $L\Delta_L^c$, $\mathcal{O}_{DW}$, and the SF-correlation function through that reentrance region in fig.5.10. $L\Delta_L^c$ between different L goes farther from each other in the DW phase, confirming it as a gapped phase (fig.5.10(a)), and (fig.5.10(c)) shows the existence of DW-order in the region. The higher Δ_L^c at $U = 6$, also shows a sign of SS-SF transition by a dip in the energy gap. Similarly, in the SF-order parameter (fig.5.10(b)), even within the finite-size lattice, we can see the decrease of Γ^α in DW-region (prominent in $r \to \infty$ limit), which again supports the reentrance.

5.7 Four-point correlation functions

Rung-leg correlation: We claim that the intra-chain superfluidity increases due to inter-chain hopping, making SS possible in ladder. Here, we show how rung-leg correlation $Rl(r = 2)$ at a distance $r = 2$ can show the signature of this mechanism. Like we discussed in section 4.3, the rung-leg correlation quantifies if one particle hops along a rung if it induces tunneling along the leg. In fig. 5.11(a), we can see that near the onset of $\mathcal{O}_{DW}$, the correlation between rung and leg for odd-rung (filled) increases, whereas on even-rung(unfilled) it decreases, as odd-rung consists of $2-2$, and even-rung of $0-0$. That is why we calculate at $r = 2$, allowing the average on odd and even rungs to be done separately. Interestingly, for larger U's, this odd-rung correlation starts decreasing earlier after it starts increasing, and this suggests that the effect of $t_\perp$ is weaker there, leading to a smaller region of SS fig.5.9. This shows that rung-leg correlation is present in SS and affects the size of the SS region in the phase diagram.

Rung-rung correlation: As we discussed above, the superfluidity is enhanced due to rung-correlation. Here, we have studied how the correlation between two rungs changes with V and U, using the rung-rung correlation defined in section-4.3. We have to remember that this correla-

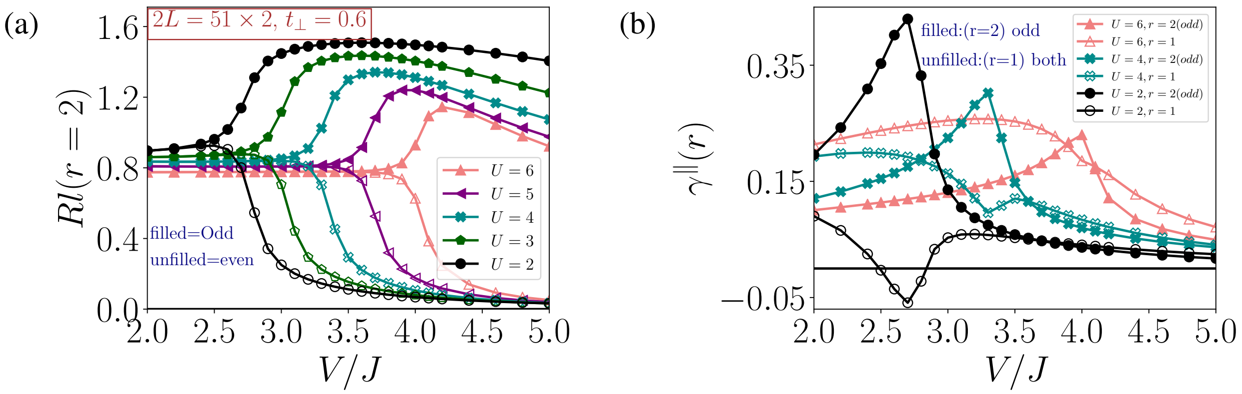

Figure 5.11: Rung-leg and rung-rung correlation for different U at $t_\perp = 0.6$: **(a)** Rung-leg correlation for odd and even rung at distance (r=2) showing larger region of odd-correlation for smaller U **(b)** Rung-rung correlation at distance r=1(odd=even) and r=2(odd)

tion has a relative directionality, i.e., if one rung particle hops from the lower to the upper leg, it should be in the opposite direction in the other rung fig.4.3. In fig.5.11(b), we can see for nearest neighbor rungs (unfilled), this correlation decreases until the $\mathscr{O}_{DW}$ arrives, which means the rung-hoppings are independent and not in the relative opposite direction in the SF phase. However, after $\mathscr{O}_{DW}$ arises, it starts growing. This can be explained by considering that if two particles are going to the same leg, they have to sit side-by-side, which is not preferable with $\mathscr{O}_{DW}$, and that is why there is a correlated hopping in a relatively opposite direction on the neighboring rungs. Contrary to that, at $r = 2$, i.e., the next-nearest neighbor rungs, the correlation decreases in SS, as it must involve two $r = 1$ processes (our model has only nearest-neighbor hopping J). That means, if in one rung particles go upward, the next rung should be downwards, implying the next nearest neighbor should go up again, making the $r = 2$ correlation smaller. The $r = 2$ at even rung-rung correlation are almost ~ 0, as there is no particle due to DW-order. One interesting observation here is : for $U = 2$, odd-correlation at (r=2) and (r=1) become equal after 3.5, which facilitates long-range coherence. We believe this can be one reason behind the larger SS region of U=2 (fig.5.9).

5.8 Phase diagram in $(t_\perp, U)$ plane for fixed V

The reentrance observed in the phase diagram for fixed $t_\perp = 0.6$ (fig.5.9) shows that along $V \simeq 4.1$, $U \in \sim [2.7, 5]$ region is in DW, whereas for other U's it is in SS. Being curious, we wonder if it is the case even with high $t_\perp$, where a DW-SS transition is expected, and the reentrance behavior would vanish. For that purpose, we draw a phase diagram in $(t_\perp, U)$ plane for fixed $V = 4.1$ (fig.5.12).

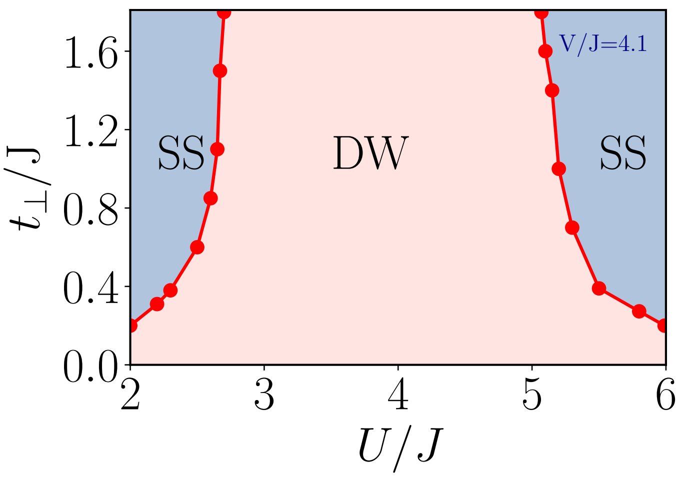

Figure 5.12: Phase diagram in $(t_\perp, U)$ plane for fixed $V = 4.1$: a reentrance of SS-DW-SS can be seen for fixed $t_\perp$. Asymptotic lines suggest for $U \in (2.7, 5)$, even with increasing $t_\perp$, there will be no SS at fixed $V = 4.1$

Surprisingly, it remains in DW for $U \in\sim [2.7, 5]$, despite providing high $t_\perp$. The slope of the SS-DW lines suggests that although for $U \simeq 2, 6$, the SS region can be extended with increasing $t_\perp$, that is not the case with $U \simeq 3, 4, 5$. Thus, it concludes that the reentrance behavior is present even with high $t_\perp$. We do not go beyond $t_\perp = 1.8$, as it needs more n_{max} to converge.

5.9 Number density

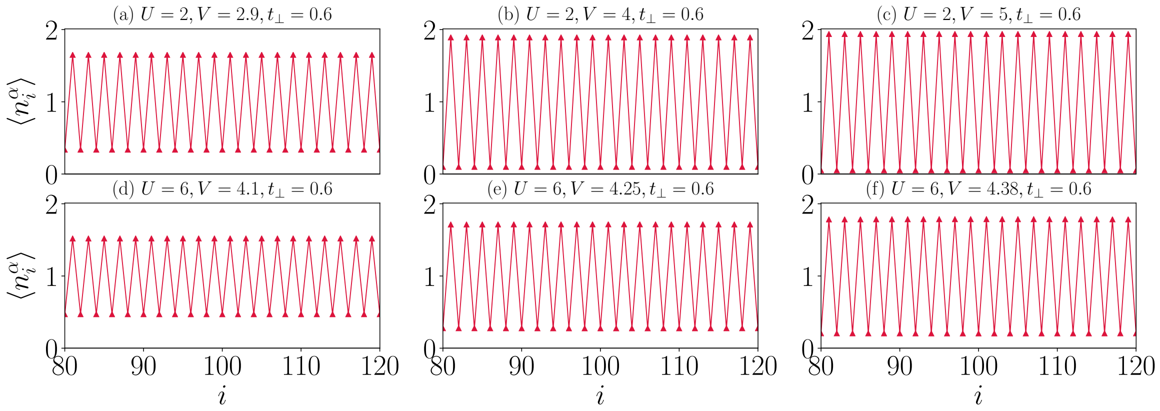

Figure 5.13: Number density in SS of U=2 and 6: **(a,d):** near SF, **(b,e):** in the middle of SS, **(c,f):** near DW

As SS phase has density-wave order, the expectation value of the number operator ($\langle \hat{n} \rangle$) shows oscillation between 0 and 2. However, it is not exactly 0 or 2, for all the parameter values. Here in fig.5.13, we can see that for $U = 2$, the amplitude of the oscillation is higher than for $U = 6$. This is expected as in strong on-site interaction (U), occupying more particles at a site is costly. Inside the SS regime, near the SF-SS transition line, the amplitude of oscillation is low and then increases with V both for U=2 and 6. We also show how does this amplitude, $|n_i - n_{i+1}|$ changes through different phases with increasing V [fig.5.14(a)] and U [fig.5.14]. In the SF phase, it is 0, and there is continuous change while going from SS to DW (fig.5.14(a)). With increasing U, for fixed V, the amplitude decreases due to competition between U and V [fig.5.14(b)].

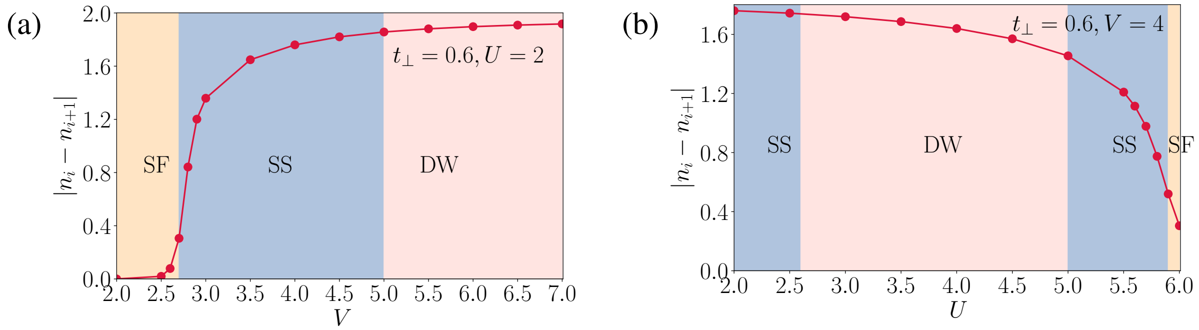

Figure 5.14: Amplitude of density-oscillation through different phases for L=61: **(a)** With increasing V, amplitude increases from zero at SF to non-zero values at SS and DW phase and then saturates, **(b)** With increasing U, amplitude decreases for fixed V

5.10 Entanglement

Entanglement in many-body physics is related to a strong correlation in the system. Thus, entanglement also contains specific signatures of the phases. Here, von Neumann entanglement along the chain and between two legs has been discussed. The entanglement spectrum shows the degeneracy at different phases.

Entanglement along the leg direction: If we bipartition the leg direction (fig.4.4(b)) into a length of l and $L - l$, the entanglement $S_l = S_{L-l}$, which means entanglement is symmetric with respect to partition. We can see in fig.5.15(a) that in the DW phase, first entanglement grows with l first, and then it saturates quickly due to short correlation length [51]. However, in SF, it has almost no l dependence due to long-range coherence and is uniform in bulk. We guess that as SS has a

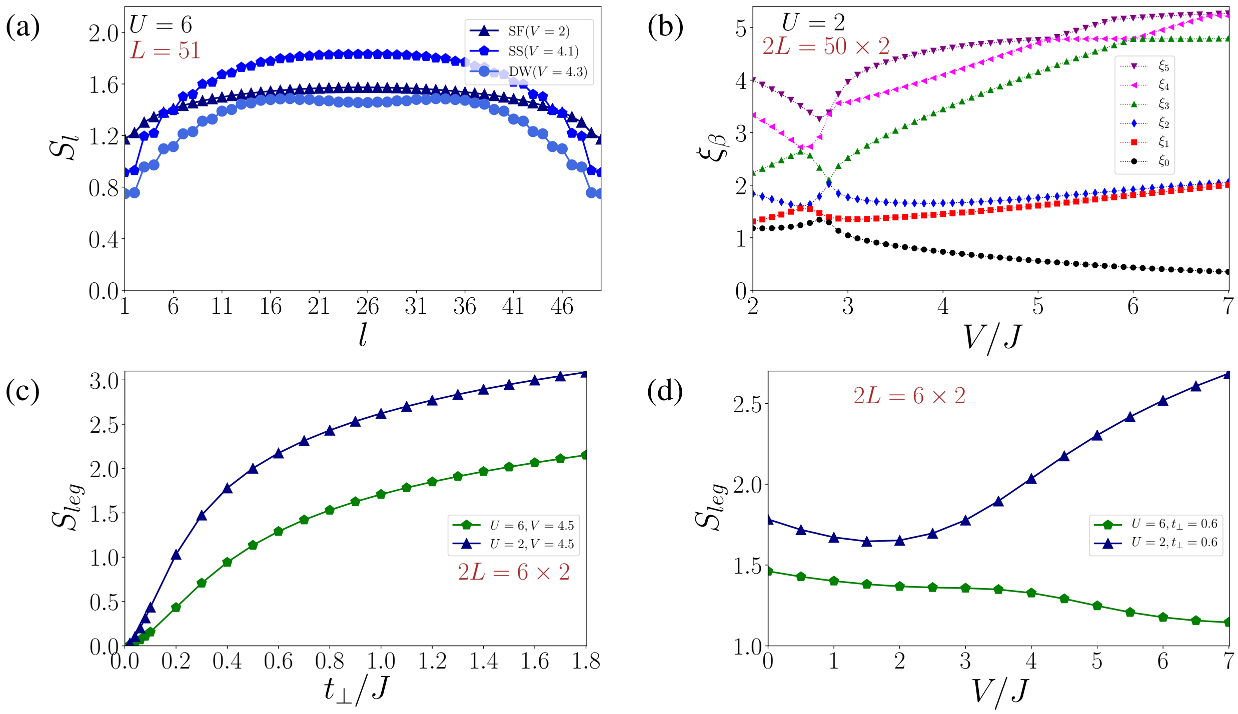

Figure 5.15: Von-Neumann entanglement and entanglement spectrum : **(a)** Entanglement along the leg-direction for SS, SF and DW, **(b)** Entanglement spectrum showing degeneracy at lowest six energies for different V, **(c)** Entanglement between two-legs with increasing $t_\perp$ for U=2,6 , **(d)** Entanglement between two-legs with increasing V for U=2,6

stronger correlation and coherence, it contains the maximum entanglement. We do not find any unique signature in SS, which can strictly distinguish it from other phases. In DW and SS phase, the effect of Z_2 symmetry breaking is also visible in the entanglement.

Entanglement between two legs: By tracing out the states in one leg (fig.4.4(a)), we calculate entanglement between two legs (S_{leg}). Taking the trace of a large Hilbert space is computationally expensive and requires very high memory. This restricts the calculation to a maximum $2L = 6 \times 2$ lattice size. However, as we want to understand how strong the legs are entangled through the rung, it should not depend much on the chain length. We observe some behavior that can be qualitatively related to the thermodynamic phase diagram. In fig.5.15(c), for fixed V=4.5, with increasing $t_\perp$, the S_{leg} increases as $t_\perp$ help to acquire more coherent superposition between legs. Although initially, S_{leg} increases fast with $t_\perp$, it slows down after a certain $t_\perp$, which is similar to the saturation behavior we observed in the phase diagrams (fig.5.1, fig.5.3(a)). We can also see that for large on-site interaction, i.e., U=6, the entanglement is smaller because it restricts the hopping of particles compared to $U = 2$.

In fig.5.15(d), we plot S_{leg} with increasing V for fixed $t_{\perp} = 0.6$. For $U = 6$, we can see a decrease in entanglement, which becomes sharp around $V \simeq 4$ (this may be the SS-DW transition point of the phase diagram). For U=2, strange behavior is observed. Although for $V < 2$, S_{leg} decreases as expected, after $V = 2$ point, it starts growing. As these plots are done for a tiny system size, we do not want to conclude or infer anything from these and recommend further studies along this line of thought.

Entanglement spectrum: From the Schmidt coefficients at the central bond of the chain (fig.4.4(b)), we calculate the entanglement spectrum using eq.4.14. To mention, here we have used $\mu = \pm 2$ at the four ends of two legs to compare with Deng *et al.* [40]. In fig.5.15(b), we have plotted the smallest six ξ_{β}, and we can see some degeneracy around V=3 and 5.5, which are near the SF-SS transition and SS-DW transition. With a larger lattice size, we expect to see better degeneracy [69]. Although we cannot identify the degenerate states here, we believe the near degeneracy of ξ_1 and ξ_2 is related to SS [40]. A further detailed study is needed in this direction.

5.11 Effect of removing rung

As we have observed in all of the above discussions, the inter-chain tunneling along the rung plays the most important role in the new physics in ladder. Although we calculated many correlation functions to understand that, another interesting way to look at this effect is: what happens if one rung is removed? Surely this will change the Hamiltonian; still, it is worth studying. We can consider many possibilities of rung removal, but for simplicity, we will discuss only one configuration by removing one central rung. First, we study the effect of V and $t_{\perp}$ as we did before in sec.5.5. Comparing to that, in fig.5.16 by removing the central rung, $\mathcal{O}_{DW}$ onsets slightly before than normal case. This is because, by removing a rung, Z_2 symmetry is already broken for that site.

However, when we draw a small phase diagram with this configuration, the difference becomes visible. In this case, there is a problem of finite-size scaling, as removing one rung, say for $L = 50$ doesn't mean that we can manage to remove $(60/50) * 1 = 6/5$ rung in $L = 60$. One can think of doubling the lattice size to $L = 100$; then we believe the configuration will have 2 removed rungs at a distance of 50 from each other, which is not what we intended to. We want a central rung removed. This is the reason we cannot go for a phase diagram in the thermodynamic limit, but at

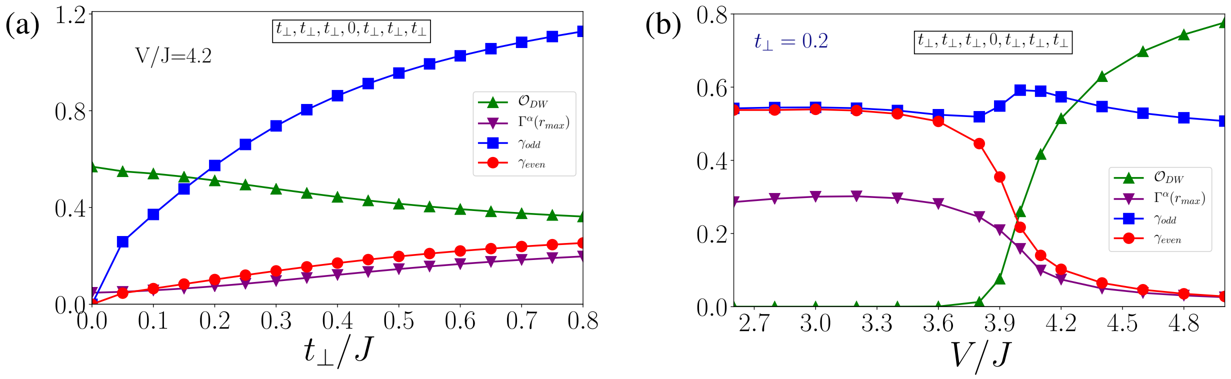

Figure 5.16: Effect of increasing $t_\perp$ and V on a lattice, where a central rung is removed: **(a)** With increasing $t_\perp$, no visible effect is observed compared to with rung case fig.5.8(a2), **(b)** With increasing V, $\mathscr{O}_{DW}$ arises before than the with rung-case fig.5.8(b1)

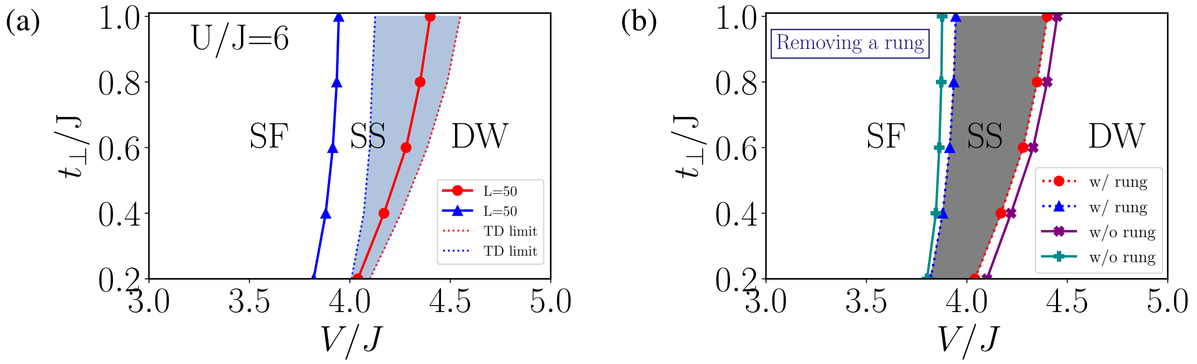

Figure 5.17: **(a)** Comparing $U = 6$ phase diagram with $L = 50$ vs in thermodynamic limit (with finite size-scaling)[shaded], **(b)** Comparing phase diagram for $U = 6$ with rung (shaded) and without a central rung

least we see the effect for $L = 50$. For that, first, we compare our thermodynamic phase diagram (fig.5.3(a)) with a phase diagram drawn for $2L = 50 \times 2$ (fig.5.17(a)). We identify local minima in the charged energy gap to obtain SS-DW transition (method-1 sec.3.2.2). In fig.5.17(a), the main difference between a finite-size and thermodynamic(TD) phase diagram is that in the TD limit, the whole diagram is pushed towards larger V_c's, and also there is a smaller region in small $t_\perp$. However, qualitatively it remains similar. With this observation, we draw a similar phase diagram but without one central rung (fig.5.17(b)), and we found more region of SS compared to the previous case, which is surprising. The SS region increases in the SF-SS transition line because $\mathscr{O}_{DW}$ arises before due to already broken local Z_2 symmetry in the removed rung site. We believe the SS-DW transition line moves towards the right due to the non-uniformity of the lattice, which prefers SS (due to fluctuation) than uniform DW.

5.12 HI phase

As we discussed previously in section 3.2.4, to get the HI phase, we need to get rid of edge mode. In this case, we have checked both methods 1 and 2 discussed in section 3.2.4, namely using $2N = 2(L+1)$ particles and $\mu = \pm 2J$ at the edges. We have to add two more particles, as we have two chains, and we have checked that adding one particle does not solve the problem. For some unknown reason, method 2 (using $\mu = \pm 2J$) in some regimes fails to arrest the decay to a negative value, so we stick to using 2(L+1) particles. Surprisingly, we have found that the HI exists only in one leg (fig.5.18), whereas all the other order parameters $\mathscr{O}_{DW}, \Gamma_{SF}$, number density remain symmetric in both chains. This also supports that HI has a *hidden* order. HI being observed only in one leg may be related to the fact that the HI phase is a topological phase in 1D, and in a ladder, it loses the necessary topology [6, 72]. For the same reason, within a very small $t_\perp$, the HI vanishes both for $U = 2$ and $U = 6$, which means that HI does not play an important role in our main phase diagrams. That's why we avoided drawing a thermodynamic phase diagram for HI.

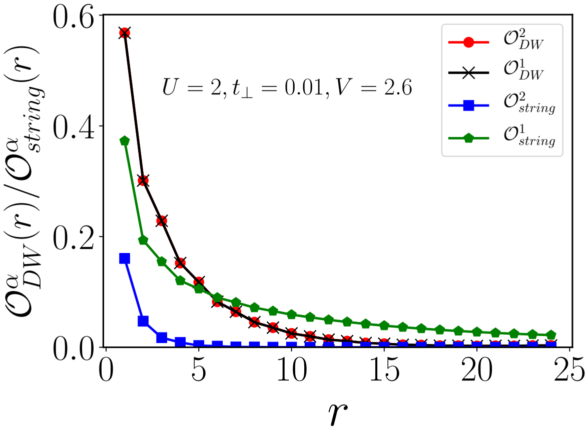

Figure 5.18: $\mathscr{O}^{\alpha}_{DW}$ and $\mathscr{O}^{\alpha}_{string}$ for both leg in HI phase: presence of HI only in one leg, whereas $\mathscr{O}_{DW}$ is symmetric in both legs

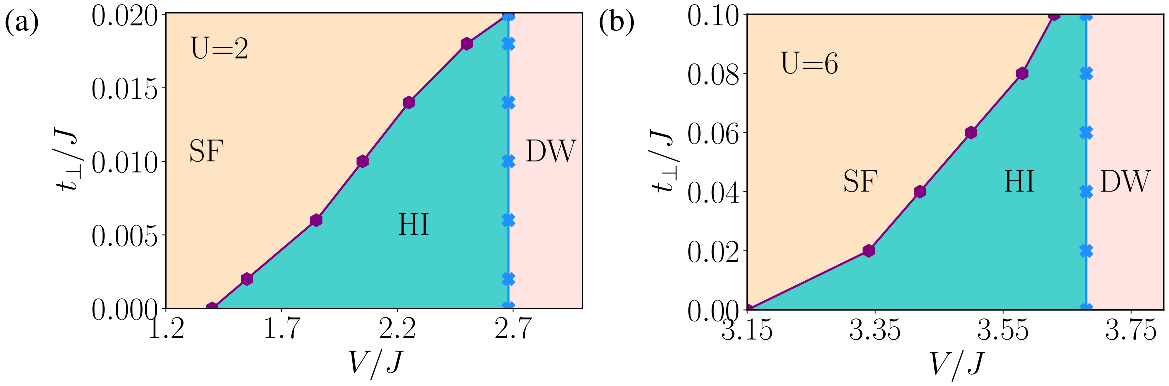

Figure 5.19: HI phase for $L = 51$ in **(a)** U=2 **(b)** U=6

Chapter 6

Conclusion and Outlook

Ultracold atoms/molecules in optical lattices offer a unique opportunity for solving various problems ranging from quantum simulation of exotic quantum many-body phases [12, 70, 73], to implementing quantum information protocols [9, 74]. The key advantage of a cold atom setup over other synthetic quantum systems is the ability to control inter-particle interactions utilizing external fields [25, 73]. In addition, due to the rapid developments in trapping/cooling techniques for atoms [38, 73, 75], the state-of-the-art experimental setups are highly versatile to realize non-trivial lattice geometries. Considering the above facts, in this thesis, we analyze the physics of a two-leg ladder extended Bose-Hubbard model using the DMRG technique. As we detail in this thesis, the model we consider is unique and can be implemented using either dipolar atoms/molecules or Rydberg admixed atoms loaded in optical lattices.

For the first time, we show the existence of a supersolid phase in a quasi-one-dimensional setup with a filling factor of $\rho = 1$, otherwise absent in 1D. We analyze the SS phase in detail using various quantities, particularly compressibility, SF, and DW order parameters. Further, we study the excitation spectrum of a superfluid and show the emergence of a roton-minima, which eventually becomes unstable at the SF-SS transition. The supersolid phase appears due to the interplay between the atom-hopping in the rungs and the nearest-neighbor interactions. Strikingly, the hopping within the rungs can induce delocalization of atoms along the chains and re-establish the coherence, which is destroyed by the strong inter-particle density-density interactions in the chain direction. We understand this process using different two-point and four-point connected correlation functions and bipartite entanglement entropy. Interestingly, the SS state is also accompanied by a reentrant transition. We observe SS-DW-SS transition as we vary the on-site interaction strength by keeping all other parameters fixed.

Besides these, we point out the effect of maximum bosons per site (n_{max}) and removal of a central rung, which can be used as extra knobs in experiments. By quenching the edge modes, we also show that the Haldane insulator (HI) exists only in one chain and have drawn a phase diagram as a function of $t_\perp$. As a whole, this thesis answers the question of dimensionality in the supersolid phase observed in the Bose-Hubbard model by extensively inspecting the role of $t_\perp$ in the ladder geometry. Our study also opens various directions in this physics of the Bose-Hubbard ladder, which we could not address due to time constraints. For instance, to get a complete understanding of the model, one should draw a 3D phase diagram in the $(t_\perp, U, V)$ plane, which we believe can show many reentrance behaviors due to competitions at different regimes. One also has to see the effect of a multi-leg ladder to describe the dimensional crossover completely. In open-chain, studying the same model with different boundary conditions is also promising as it can give rise to other phases [15, 41]. As a novelty of our model, the model we consider here can be realized in a single chain with atoms occupying two bands instead of one [76]. We also wonder how a disorder will flow through the ladder in different phases. As a basic query, one can also investigate the quantum quench dynamics through the reentrant region, including the Kibble-Zurek mechanism [77–80].

Appendix A

Density Matrix Renormalization Group

In quantum many-body physics, quantum fluctuation and correlation play the most critical roles. To study the robust quantum phases in those microscopic models, large-scale numerical simulations are essential, especially when our favorite mean-field theory fails. The main difficulty here comes from that the large Hilbert space spanned by the micro-states grows with the system size, and the classical computer has limited storage. In this case, simulations based on tensor-product state (TNS) based methods are proven to be very efficient and powerful. One of the most successful ones is the density-matrix renormalization group (DMRG) [29,81,82]. Although DMRG originally started in the 1D system, after realizing its success, the idea is extrapolated to a quasi-1D system, where we can effectively map it to a 1D lattice (fig.4.2). DMRG 's success is related to the fact that quantum ground states of our interest are often only slightly entangled (area law), for which it can be represented efficiently using matrix-product states (MPS) [11].

Area Law: Although a "typical" state in the Hilbert space shows a volume law [Entanglement $\propto$ Volume(partitions)], ground states $|\psi_0\rangle$ of gapped local Hamiltonians follow area law i.e. the entanglement entropy grows proportionally with the area of the cut [48]. This is related to the

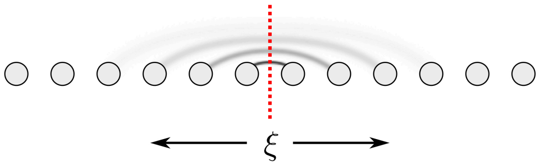

Figure A.1: Area law: significant fluctuations in gapped states occur only on short-range scales (taken from [68]) fact that in gapped ground states fluctuations are only within the correlation length ξ (fig.A.1). So for $N \geq \xi$, the entanglement does not grow, and hence only degrees of freedom near the cut are entangled.

This slight entanglement of states can be captured in a relatively *small* number of Schmidt states, and that in turn partially solves the storage problem of large Hilbert space. Thus we can truncate the Schmidt decomposition at some finite χ for all $\varepsilon > 0$ such that

$$\left|\left| |\psi\rangle - \underbrace{\sum_{\alpha=1}^{\chi} \Lambda_\alpha |\alpha\rangle_{\text{left}} \otimes |\alpha\rangle_{\text{right}}}_{|\psi\rangle_{\text{trunc}}} \right|\right| < \varepsilon \tag{A.1}$$

The *truncation error* is defined as the total Schmidt probability of discarded states, i.e. $(1 - \sum_{\alpha=1}^{\chi} \Lambda_\alpha^2)$.

Matrix Product States (MPS): We define the local basis on site j by $|n_j\rangle$ with $n_j = 0, 1, .., n_{max}$, where n_{max} is the maximum number of bosons allowed per site. In this basis, a generic pure quantum state of lattice size of L can be written as :

$$|\psi\rangle = \sum_{n_1,n_2,....,n_L} \psi_{n_1,n_2,......,n_L} |n_1, n_2, ..., n_L\rangle \tag{A.2}$$

MPS is an ansatz for $\psi_{n_1,n_2,......,n_L}$, where it is decomposed as a product of matrices [68, 83]-

$$\psi_{n_1,n_2,......,n_L} = \sum_{\alpha_2,.....\alpha_L} M^{[1]n_1}_{\alpha_1\alpha_2} M^{[2]n_2}_{\alpha_2\alpha_3} .... M^{[L]n_L}_{\alpha_L\alpha_{L+1}} \equiv M^{[1]n_1} M^{[2]n_2} .... M^{[L]n_L} \tag{A.3}$$

Each $M^{[j]n_j}$ is a $\chi_j \times \chi_{j+1}$ dimensional matrix, where j is the site index, and α_j are called *bond* or *auxiliary* indices, which is bounded by *bond-dimension* of χ_j. This χ_j defines the maximum allowed entanglement between $|n_{j-1}\rangle$ and $|n_j\rangle$. Although by using arbitrary χ_j, we can represent any state, we *truncate* it to maximum bond-dimension χ_{max} for computational limitation.

Matrix Product Operators (MPO): To use MPS for diagonalization, the Hamiltonian has to be expressed in MPO, which is a generalization of MPS to operators, written as

$$O = \sum_{\substack{n_1,....,n_L \\ n'_1,....,n'_L}} v^{\text{left}}\, W^{[1]n_1 n'_1} W^{[2]n_2 n'_2} .... W^{[L]n_L n'_L}\, v^{\text{right}} |n_1, n_2, ..., n_L\rangle \langle n'_1, n'_2, ..., n'_L| \tag{A.4}$$

where $W^{[j]n_j n'_j}$ are $D \times D$ matrices and $v^{\text{left(right)}}$ are left(right) vectors. We translate the Hamiltonian to MPO form like a finite state machine [84, 85].

Density Matrix Renormalization Group (DMRG): DMRG [29] is a variational algorithm for optimizing the MPS to get the eigenstates of the Hamiltonian (H written as MPO). We start with an initial MPS of $|\psi\rangle$, and variationally optimize the tensor product of two neighboring sites(eg.- j and $j+1$) using the Lanczos method to obtain the ground state energy from $\langle\psi|H|\psi\rangle$, while the rest of the chain is kept fixed. For this purpose, the H is projected in $\{|\alpha_j\rangle_{\text{left}} \otimes |n_j\rangle \otimes |n_{j+1}\rangle \otimes |\alpha_{j+2}\rangle_{\text{right}}\}$ basis. We repeat this two-site update for all neighboring sites in the lattice in sequential order from left to right and again come back from right to left. This is called one *sweep*. With an increasing number of sweeps, the energy converges.

Charge conservation: As we work with a fixed number of atoms, all the tensor has to be in the same number sector (block) of the Hamiltonian. By using a *charge rule* [68], we can selectively disappear entries to ensure the block structure of each tensor individually.

To give an example, consider that the total number of particles at a two-site lattice is N, and there should be no process in the Hamiltonian that change the total number, i.e.

$$H_{m_1 m_2 n_1 n_2} = 0 \text{ if } m_1 + m_2 \neq n_1 + n_2 \tag{A.5}$$

where the Hamiltonian has the form $H = \sum_{m_1,m_2,n_1,n_2} H_{m_1 m_2 n_1 n_2} |m_1\rangle|m_2\rangle\langle n_1|\langle n_2|$. This means we should always choose those special bra and ket states for charge conservation. As we use MPS tensors to represent those states, here we will discuss how to implement a charge-rule for an arbitrary l-leg tensor M. We first assign one sign $\zeta^{[i]} = \pm 1$ for each leg a_i ($i \in [1, l]$), in particular, $\zeta = +1 (\zeta = -1)$ for a ket (bra). We also define the charge of leg-a_i as q_{a_i}. Now, if we fix the total charge of the tensor as Q, then the charge rule reads as

$$\forall a_1, a_2 .... a_l : \quad \zeta^{[1]} q^{[1]}_{a_1} + \zeta^{[2]} q^{[2]}_{a_2} + ... + \zeta^{[l]} q^{[l]}_{a_l} \neq Q \Rightarrow M_{a_1 a_2 ... a_l} = 0 \tag{A.6}$$

Charged Energy Gap: As we run DMRG simulations for the fixed total number of particles (total charge); in order to calculate charged energy gap Δ^c_L $(= E^0_L(N+1) + E^0_L(N-1) - 2E^0_L(N))$, we need to run three instances of DMRG, each of them separately targeting the ground state with $\{N, N \pm 1\}$ particle number sectors [3].

DMRG vs QMC: As the quantum Monte-Carlo method does not suffer from any sign problem in the bosonic system, QMC is also a good method for diagonalization. However, in our thesis, we largely depend on the charged-energy gap and finite-size scaling, which is easier in DMRG than QMC [5]. Also, in DMRG by restricting maximum bond-dimension, we can systematically study the role of entanglement in particular phases and phase transitions [35].

Appendix B

Optical Lattice

A periodic potential in the experiment can be formed by overlapping two counter-propagating laser beams, where the interference between lasers creates an optical standing wave with periodicity $\lambda_L/2$ (fig.2.2) [75]. These are called optical lattices. Depending on the number of lasers, 1D, 2D, 3D periodic potentials can be obtained. As an example, pair of laser beams can effectively create the 1D lattice, which is an array of 2D-disk-like traps (fig.B.1). Such periodic potential has the form

$$V_{lat}(x) = V_0 \sin^2(k_L x) \tag{B.1}$$

where V_0 is the potential depth, given in the units of recoil energy $E_R = \hbar^2 k_L^2/2m$. The laser is far-detuned from the atomic resonant frequency to protect atoms from spontaneous emission, creating pure conservative and defect-free potentials [73]. Neutral atoms in such potential have two kinds of motions [20]-

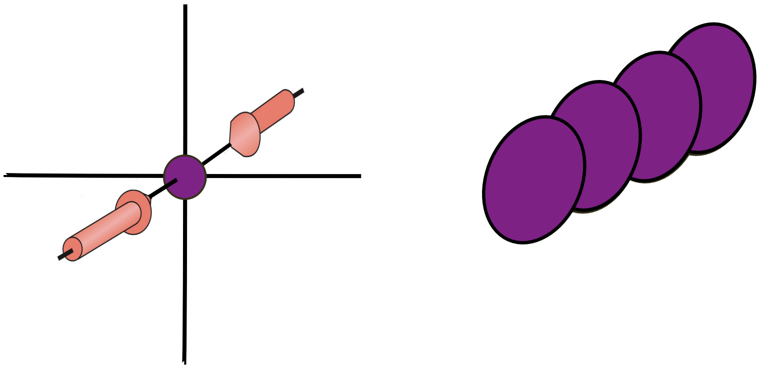

Figure B.1: **Left:** 1D optical lattice formed by pair of laser beams, where **(Right:)** the atoms are confined to 2D potential disks

(a) vibrational motion within an individual potential well: U

(b) tunneling between neighboring wells: J

If we increase the depth of the optical potential, the atomic wave function becomes more localized, increasing the onsite repulsion, and at the same time, tunneling decreases (U/J increases). At ultracold temperature, neutral atoms typically interact only by s-wave scattering, which can be represented by a short-range and isotropic pseudo-potential [12,86]:

$$V(r-r') = \frac{4\pi\hbar^2 a_s}{m}\delta(r) \equiv g\delta(r) \tag{B.2}$$

where a_S is the s-wave scattering length of an atom. This leads to (using 2.4), $U = \frac{4\pi\hbar^2 a_s}{m}\int dx|w_0(x)|^4$, which creates a BHM in the experiment [25]. The coherence in SF can be measured by looking at the interference pattern formed by freely expanding atoms. The charged gap can be calculated using the excitation spectrum in MI. This is done by tilting the neighboring lattice potential (fig.B.2) such that when both sites became equal in energy the particle hops. This offset in energy is then the same as charged energy gap as we explained in sec.2.2.2.

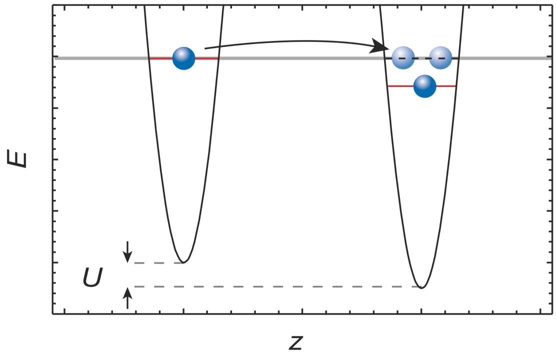

Figure B.2: Measuring energy gap: potential gradient along z-direction can diminish the energy difference between neighboring sites allowing the atoms to tunnel (taken from Fig.4b of Ref. [25]).

Bibliography

[1] Mehran Kardar. *Statistical Physics of Fields*. Cambridge University Press, 2007.

[2] Subir Sachdev. Quantum phase transitions. *Handbook of Magnetism and Advanced Magnetic Materials*, 2007.

[3] Davide Rossini and Rosario Fazio. Phase diagram of the extended bose–hubbard model. *New Journal of Physics*, 14(6):065012, 2012.

[4] GG Batrouni, RT Scalettar, GT Zimanyi, and Arno P Kampf. Supersolids in the bose-hubbard hamiltonian. *Physical review letters*, 74(13):2527, 1995.

[5] GG Batrouni, VG Rousseau, RT Scalettar, and B Grémaud. Competition between the haldane insulator, superfluid and supersolid phases in the one-dimensional bosonic hubbard model. In *Journal of Physics: Conference Series*, volume 640, page 012042. IOP Publishing, 2015.

[6] Erez Berg, Emanuele G Dalla Torre, Thierry Giamarchi, and Ehud Altman. Rise and fall of hidden string order of lattice bosons. *Physical Review B*, 77(24):245119, 2008.

[7] MA Cazalilla, Roberta Citro, Thierry Giamarchi, Edmond Orignac, and Marcos Rigol. One dimensional bosons: From condensed matter systems to ultracold gases. *Reviews of Modern Physics*, 83(4):1405, 2011.

[8] Hendrik Weimer, Markus Müller, Igor Lesanovsky, Peter Zoller, and Hans Peter Büchler. A rydberg quantum simulator. *Nature Physics*, 6:382–388, 2010.

[9] Valentin Kasper, Daniel González-Cuadra, Apoorva Hegde, Andy Xia, Alexandre Dauphin, Felix Huber, Eberhard Tiemann, Maciej Lewenstein, Fred Jendrzejewski, and Philipp Hauke. Universal quantum computation and quantum error correction with ultracold atomic mixtures. *arXiv preprint arXiv:2010.15923*, 2020.

[10] Meetu Sethi Luthra, Tapan Mishra, Ramesh V Pai, and BP Das. Phase diagram of a bosonic ladder with two coupled chains. *Physical Review B*, 78(16):165104, 2008.

[11] Ulrich Schollwöck. The density-matrix renormalization group in the age of matrix product states. *Annals of physics*, 326(1):96–192, 2011.

[12] Maciej Lewenstein, Anna Sanpera, and Veronica Ahufinger. *Ultracold Atoms in Optical Lattices: Simulating quantum many-body systems*. Oxford University Press, 2012.

[13] Till D Kühner and H Monien. Phases of the one-dimensional bose-hubbard model. *Physical Review B*, 58(22):R14741, 1998.

[14] Ramesh V Pai, Rahul Pandit, HR Krishnamurthy, and S Ramasesha. One-dimensional disordered bosonic hubbard model: A density-matrix renormalization group study. *Physical review letters*, 76(16):2937, 1996.

[15] Jamshid Moradi Kurdestany, Ramesh V Pai, Subroto Mukerjee, and Rahul Pandit. Phases, transitions, and patterns in the one-dimensional extended bose-hubbard model. *arXiv*, pages arXiv–1403, 2014.

[16] Thierry Lahaye, C Menotti, L Santos, M Lewenstein, and T Pfau. The physics of dipolar bosonic quantum gases. *Reports on Progress in Physics*, 72(12):126401, 2009.

[17] Alexander W Glaetzle, Marcello Dalmonte, Rejish Nath, Ioannis Rousochatzakis, Roderich Moessner, and Peter Zoller. Quantum spin-ice and dimer models with rydberg atoms. *Physical Review X*, 4(4):041037, 2014.

[18] N Elstner and H Monien. Dynamics and thermodynamics of the bose-hubbard model. *Physical Review B*, 59(19):12184, 1999.

[19] Matthew PA Fisher, Peter B Weichman, Geoffrey Grinstein, and Daniel S Fisher. Boson localization and the superfluid-insulator transition. *Physical Review B*, 40(1):546, 1989.

[20] Dieter Jaksch, Christoph Bruder, Juan Ignacio Cirac, Crispin W Gardiner, and Peter Zoller. Cold bosonic atoms in optical lattices. *Physical Review Letters*, 81(15):3108, 1998.

[21] Neil W Ashcroft, N David Mermin, et al. *Solid state physics*, volume 2005. holt, rinehart and winston, new york London, 1976.

[22] Mark Kremer, Rashi Sachdeva, Albert Benseny, and Thomas Busch. Interaction-induced effects on bose-hubbard parameters. *Physical Review A*, 96(6):063611, 2017.

[23] Henk TC Stoof, Koos B Gubbels, and Dennis Dickerscheid. *Ultracold quantum fields*. Springer, 2009.

[24] Yashwant Chougale and Rejish Nath. Ab initio calculation of hubbard parameters for rydberg-dressed atoms in a one-dimensional optical lattice. *Journal of Physics B: Atomic, Molecular and Optical Physics*, 49(14):144005, 2016.

[25] Markus Greiner, Olaf Mandel, Tilman Esslinger, Theodor W Hänsch, and Immanuel Bloch. Quantum phase transition from a superfluid to a mott insulator in a gas of ultracold atoms. *nature*, 415(6867):39–44, 2002.

[26] Antoine Georges and Thierry Giamarchi. Strongly correlated bosons and fermions in optical lattices. *arXiv preprint arXiv:1308.2684*, 2013.

[27] Thierry Giamarchi. *Quantum physics in one dimension*, volume 121. Clarendon press, 2003.

[28] T Giamarchi and Oxford University Press. *Quantum Physics in One Dimension*. Clarendon Press, 2004.

[29] Steven R White. Density matrix formulation for quantum renormalization groups. *Physical review letters*, 69(19):2863, 1992.

[30] H Monien and T D Ku. Phases of the one-dimensional bose-hubbard model ¨. 58:741–744, 1998.

[31] Till D Kühner, Steven R White, and Hartmut Monien. One-dimensional bose-hubbard model with nearest-neighbor interaction. *Physical Review B*, 61(18):12474, 2000.

[32] Ramesh V Pai and Rahul Pandit. Superfluid, mott-insulator, and mass-density-wave phases in the one-dimensional extended bose-hubbard model. *Physical Review B*, 71(10):104508, 2005.

[33] S. Ejima, H. Fehske, and F. Gebhard. Dynamic properties of the one-dimensional bose-hubbard model. *Epl*, 93, 2011.

[34] Ramamurti Shankar. *Quantum Field Theory and Condensed Matter: An Introduction*. Cambridge University Press, 2017.

[35] M Pino, J Prior, AM Somoza, D Jaksch, and SR Clark. Reentrance and entanglement in the one-dimensional bose-hubbard model. *Physical Review A*, 86(2):023631, 2012.

[36] Krzysztof Góral, Luis Santos, and Maciej Lewenstein. Quantum phases of dipolar bosons in optical lattices. *Physical Review Letters*, 88(17):170406, 2002.

[37] Tomasz Sowiński, Omjyoti Dutta, Philipp Hauke, Luca Tagliacozzo, and Maciej Lewenstein. Dipolar molecules in optical lattices. *Physical review letters*, 108(11):115301, 2012.

[38] J Stuhler, A Griesmaier, T Koch, M Fattori, T Pfau, S Giovanazzi, P Pedri, and L Santos. Observation of dipole-dipole interaction in a degenerate quantum gas dd (r). 150406:1–4, 2005.

[39] Roman Krems, Bretislav Friedrich, and William C Stwalley. *Cold molecules: theory, experiment, applications*. CRC press, 2009.

[40] Xiaolong Deng and Luis Santos. Entanglement spectrum of one-dimensional extended bose-hubbard models. *Physical Review B*, 84(8):085138, 2011.

[41] Sebastian Stumper and Junichi Okamoto. Macroscopic boundary effects in the one-dimensional extended bose-hubbard model. *arXiv preprint arXiv:2001.04790*, 2020.

[42] Emanuele G Dalla Torre, Erez Berg, and Ehud Altman. Hidden order in 1d bose insulators. *Physical review letters*, 97(26):260401, 2006.

[43] F Duncan M Haldane. Nonlinear field theory of large-spin heisenberg antiferromagnets: semiclassically quantized solitons of the one-dimensional easy-axis néel state. *Physical Review Letters*, 50(15):1153, 1983.

[44] Tom Kennedy and Hal Tasaki. Hidden z 2× z 2 symmetry breaking in haldane-gap antiferromagnets. *Physical review b*, 45(1):304, 1992.

[45] FDM Haldane. Effective harmonic-fluid approach to low-energy properties of one-dimensional quantum fluids. *Physical Review Letters*, 47(25):1840, 1981.

[46] Hirotsugu Matsuda and Toshihiko Tsuneto. Off-diagonal long-range order in solids. *Progress of Theoretical Physics Supplement*, 46:411–436, 1970.

[47] Parhat Niyaz, RT Scalettar, CY Fong, and GG Batrouni. Phase transitions in an interacting boson model with near-neighbor repulsion. *Physical Review B*, 50(1):362, 1994.

[48] Matthew B Hastings. An area law for one-dimensional quantum systems. *Journal of Statistical Mechanics: Theory and Experiment*, 2007(08):P08024, 2007.

[49] Krzysztof Biedroń, Mateusz Łacki, and Jakub Zakrzewski. Extended bose-hubbard model with dipolar and contact interactions. *Physical Review B*, 97(24):245102, 2018.

[50] Tapan Mishra, Ramesh V Pai, and BP Das. Induced supersolidity in a mixture of normal and hard-core bosons. *Physical Review B*, 81(2):024503, 2010.

[51] Jamshid Moradi Kurdestany, Ramesh V. Pai, Subroto Mukerjee, and Rahul Pandit. Phases, transitions, and patterns in the one-dimensional extended bose-hubbard model. 3 2014.

[52] Tom Kennedy. Exact diagonalisations of open spin-1 chains. *Journal of Physics: Condensed Matter*, 2(26):5737, 1990.

[53] Tapan Mishra, Ramesh V Pai, S Ramanan, Meetu Sethi Luthra, and BP Das. Supersolid and solitonic phases in the one-dimensional extended bose-hubbard model. *Physical Review A*, 80(4):043614, 2009.

[54] Takahiro Ohgoe, Takafumi Suzuki, and Naoki Kawashima. Ground-state phase diagram of the two-dimensional extended bose-hubbard model. *Physical Review B*, 86(5):054520, 2012.

[55] Soumik Bandyopadhyay, Rukmani Bai, Sukla Pal, K Suthar, Rejish Nath, and D Angom. Quantum phases of canted dipolar bosons in a two-dimensional square optical lattice. *Physical Review A*, 100(5):053623, 2019.

[56] GG Batrouni, F Hébert, and RT Scalettar. Supersolid phases in the one-dimensional extended soft-core bosonic hubbard model. *Physical review letters*, 97(8):087209, 2006.

[57] Jonathan M. Fellows and Sam T. Carr. Superfluid, solid, and supersolid phases of dipolar bosons in a quasi-one-dimensional optical lattice. *Physical Review A - Atomic, Molecular, and Optical Physics*, 84, 11 2011.

[58] M. Iskin. Route to supersolidity for the extended bose-hubbard model. *Physical Review A - Atomic, Molecular, and Optical Physics*, 83:0–4, 2011.

[59] Michael E Fisher, Michael N Barber, and David Jasnow. Helicity modulus, superfluidity, and scaling in isotropic systems. *Physical Review A*, 8(2):1111, 1973.

[60] P Donohue and T Giamarchi. Mott-superfluid transition in bosonic ladders. *Physical Review B*, 63(18):180508, 2001.

[61] Manpreet Singh, Tapan Mishra, Ramesh V Pai, and BP Das. Quantum phases of attractive bosons on a bose-hubbard ladder with three-body constraint. *Physical Review A*, 90(1):013625, 2014.

[62] Bradraj Pandey, S Sinha, and Swapan K Pati. Quantum phases of hardcore bosons in two coupled chains: A density matrix renormalization group study. *Physical Review B*, 91(21):214432, 2015.

[63] Manpreet Singh, Suman Mondal, BK Sahoo, and Tapan Mishra. Quantum phases of constrained dipolar bosons in coupled one-dimensional optical lattices. *Physical Review A*, 96(5):053604, 2017.

[64] A Argüelles and L Santos. Mott-insulator phases of nonlocally coupled one-dimensional dipolar bose gases. *Physical Review A*, 75(5):053613, 2007.

[65] Haiming Deng, Hui Dai, Jiahao Huang, Xizhou Qin, Jun Xu, Honghua Zhong, Chunshan He, Chaohong Lee, et al. Cluster gutzwiller study of the bose-hubbard ladder: Ground-state phase diagram and many-body landau-zener dynamics. *Physical Review A*, 92(2):023618, 2015.

[66] Shang-Shu Li, Zi-Yong Ge, and Heng Fan. Localization of rung pairs in hard-core bose-hubbard ladder. *arXiv preprint arXiv:2005.08530*, 2020.

[67] Ulrich Schollwöck. The density-matrix renormalization group. *Reviews of modern physics*, 77(1):259, 2005.

[68] Johannes Hauschild and Frank Pollmann. Efficient numerical simulations with tensor networks: Tensor network python (tenpy). *SciPost Physics Lecture Notes*, 2018.

[69] Satoshi Ejima, Florian Lange, and Holger Fehske. Spectral and entanglement properties of the bosonic haldane insulator. *Physical review letters*, 113(2):020401, 2014.

[70] Immanuel Bloch, Jean Dalibard, and Wilhelm Zwerger. Many-body physics with ultracold gases. *Reviews of modern physics*, 80(3):885, 2008.

[71] M Iskin. Route to supersolidity for the extended bose-hubbard model. *Physical Review A*, 83(5):051606, 2011.

[72] F. Anfuso and A. Rosch. Fragility of string orders. *Physical Review B - Condensed Matter and Materials Physics*, 76:1–6, 2007.

[73] Immanuel Bloch, Jean Dalibard, and Sylvain Nascimbene. Quantum simulations with ultracold quantum gases. *Nature Physics*, 8(4):267–276, 2012.

[74] D Jaksch, JI Cirac, P Zoller, SL Rolston, R Côté, and MD Lukin. Fast quantum gates for neutral atoms. *Physical Review Letters*, 85(10):2208, 2000.

[75] Immanuel Bloch. Ultracold quantum gases in optical lattices. *Nature physics*, 1(1):23–30, 2005.

[76] Omjyoti Dutta, Mariusz Gajda, Philipp Hauke, Maciej Lewenstein, Dirk-Sören Lühmann, Boris A Malomed, Tomasz Sowiński, and Jakub Zakrzewski. Non-standard hubbard models in optical lattices: a review. *Reports on Progress in Physics*, 78(6):066001, 2015.

[77] Wojciech H Zurek, Uwe Dorner, and Peter Zoller. Dynamics of a quantum phase transition. *Physical review letters*, 95(10):105701, 2005.

[78] Jacek Dziarmaga. Dynamics of a quantum phase transition and relaxation to a steady state. 12 2009.

[79] Keita Shimizu, Yoshihito Kuno, Takahiro Hirano, and Ikuo Ichinose. Dynamics of a quantum phase transition in the bose-hubbard model: Kibble-zurek mechanism and beyond. *Physical Review A*, 97(3):033626, 2018.

[80] Mauro Schiulaz, E. Jonathan Torres-Herrera, and Lea F. Santos. Thouless and relaxation time scales in many-body quantum systems. *Physical Review B*, 99, 5 2019.

[81] André Luiz Malvezzi. An introduction to numerical methods in low-dimensional quantum systems, 2003.

[82] Adrian E. Feiguin. The density matrix renormalization group and its time-dependent variants. *AIP Conference Proceedings*, 1419:5–92, 2011.

[83] Stellan Östlund and Stefan Rommer. Thermodynamic limit of density matrix renormalization. *Physical review letters*, 75(19):3537, 1995.

[84] Gregory M Crosswhite and Dave Bacon. Finite automata for caching in matrix product algorithms. *Physical Review A*, 78(1):012356, 2008.

[85] Florian Fröwis, Volckmar Nebendahl, and Wolfgang Dür. Tensor operators: Constructions and applications for long-range interaction systems. *Physical Review A*, 81(6):062337, 2010.

[86] Kerson Huang and Chen Ning Yang. Quantum-mechanical many-body problem with hard-sphere interaction. *Physical review*, 105(3):767, 1957.